

Orbital and Atmospheric Characterization of the 1RXS J034231.8+121622 System using High-resolution Spectroscopy Confirms that the Companion is a Low-mass Star

Clarissa R. Do ¹ , Ben Sappey ¹ , Quinn M. Konopacky ² , Jean-Baptiste Ruffio ² , Kelly K. O’Neil ³ , Tuan Do ⁴ , Gregory Martinez ⁴ , Travis S. Barman ⁵ , Jayke S. Nguyen ² , Jerry W. Xuan ⁶ , Christopher A. Theissen ² , Sarah Blunt ⁷ , William Thompson ⁸ , Chih-Chun Hsu ⁷ , Ashley Baker ⁶, Randall Bartos ⁹, Geoffrey A. Blake ¹⁰ , Benjamin Calvin ^{4,6} , Sylvain Cetre ¹¹ , Jacques-Robert Delorme ¹¹ , Greg Doppmann ¹¹ , Daniel Echeverri ⁶ , Luke Finnerty ⁴ , Michael P. Fitzgerald ⁴ , Julie Inglis ¹⁰ , Nemanja Jovanovic ⁶ , Ronald A. López ⁴ , Dimitri Mawet ^{6,9} , Evan Morris ¹² , Jacklyn Pezzato ⁶, Tobias Schofield ⁶, Andrew Skemer ¹² , J. Kent Wallace ⁹ , Jason J. Wang ⁷ , Ji Wang ¹³ , and Joshua Liberman ¹⁴ 

¹ Department of Physics, University of California, San Diego, La Jolla, CA 92093, USA

² Department of Astronomy and Astrophysics, University of California, San Diego, La Jolla, CA 92093, USA

³ Department of Physics, University of Nevada, Reno, Reno, NV 89557, USA

⁴ Department of Physics & Astronomy, 430 Portola Plaza, University of California, Los Angeles, CA 90095, USA

⁵ Lunar and Planetary Laboratory, University of Arizona, Tucson, AZ 85721, USA

⁶ Department of Astronomy, California Institute of Technology, Pasadena, CA 91125, USA

⁷ Center for Interdisciplinary Exploration and Research in Astrophysics (CIERA) and Department of Physics and Astronomy, Northwestern University, Evanston, IL 60208, USA

⁸ National Research Council of Canada Herzberg, 5071 West Saanich Rd., Victoria, BC, V9E 2E7, Canada

⁹ Jet Propulsion Laboratory, California Institute of Technology, 4800 Oak Grove Dr., Pasadena, CA 91109, USA

¹⁰ Division of Geological & Planetary Sciences, California Institute of Technology, Pasadena, CA 91125, USA

¹¹ W. M. Keck Observatory, 65-1120 Mamalahoa Hwy., Kamuela, HI, USA

¹² Department of Astronomy & Astrophysics, University of California, Santa Cruz, CA 95064, USA

¹³ Department of Astronomy, The Ohio State University, 100 W 18th Ave., Columbus, OH 43210, USA

¹⁴ James C. Wyant College of Optical Sciences, University of Arizona, Meinel Building 1630 E. University Blvd., Tucson, AZ, 85721, USA

Received 2024 February 20; revised 2024 April 9; accepted 2024 April 10; published 2024 May 22

Abstract

The 1RXS J034231.8+121622 system consists of an M dwarf primary and a directly imaged low-mass stellar companion. We use high-resolution spectroscopic data from Keck/KPIC to estimate the objects’ atmospheric parameters and radial velocities (RVs). Using PHOENIX stellar models, we find that the primary has a temperature of 3460 ± 50 K and a metallicity of 0.16 ± 0.04 , while the secondary has a temperature of 2510 ± 50 K and a metallicity of $0.13^{+0.12}_{-0.11}$. Recent work suggests this system is associated with the Hyades, giving it an older age than previous estimates. Both metallicities agree with current Hyades [Fe/H] measurements (0.11–0.21). Using stellar evolutionary models, we obtain significantly higher masses for the objects, $0.30 \pm 0.15 M_{\odot}$ and $0.08 \pm 0.01 M_{\odot}$ ($84 \pm 11 M_{Jup}$), respectively. Using the RVs and a new astrometry point from Keck/NIRC2, we find that the system is likely an edge-on, moderately eccentric ($0.41^{+0.27}_{-0.08}$) configuration. We also estimate the C/O ratio of both objects using custom grid models, obtaining 0.42 ± 0.10 (primary) and 0.55 ± 0.10 (companion). From these results, we confirm that this system most likely went through a binary star formation process in the Hyades. The significant changes in this system’s parameters since its discovery highlight the importance of high-resolution spectroscopy for both orbital and atmospheric characterization of directly imaged companions.

Unified Astronomy Thesaurus concepts: Brown dwarfs (185); Direct imaging (387); High resolution spectroscopy (2096); Exoplanets (498); Binary stars (154); Orbit determination (1175); Atmospheric composition (2120); Star formation (1569); Exoplanet formation (492)

1. Introduction

Directly imaging substellar companions allows for the observation of the companion’s thermally emitted light. This method of detection allows for their orbital and atmospheric characterization, providing valuable information on how these objects formed. The observation of these objects using ground-based telescopes such as the W. M. Keck Observatory requires an adaptive optics system (AO) coupled with an imaging instrument to obtain relative companion astrometry for orbital characterization and a medium- or high-resolution spectrograph to obtain

relative radial velocities (RVs) for further orbital characterization and spectral information on the companion.

Temperature, $\log(g)$, rotation speed, bulk metallicity, and elemental abundances that may be tracers of formation processes in these systems can be gleaned from spectra of the companion and host star. Temperature, $\log(g)$, and luminosity values coupled with a system’s age are useful for inferring the mass of an object using evolutionary models (e.g., Baraffe et al. 1998, 2003, 2015; Morley et al. 2024; Mukherjee et al. 2024).

Beyond these quantities, high-resolution spectroscopy ($R > 20,000$) can offer a means to measure elemental abundances, such as of carbon and oxygen, and chemical ratios of these abundances by resolving individual absorption lines from different molecules containing these elements. All of these parameters can inform how these directly imaged companions



Original content from this work may be used under the terms of the [Creative Commons Attribution 4.0 licence](#). Any further distribution of this work must maintain attribution to the author(s) and the title of the work, journal citation and DOI.

have formed and whether they are exoplanets, brown dwarfs, or low-mass stars. Therefore, directly imaging both high- and low-mass companions is important for better constraining and informing companion formation trends.

Obtaining high-resolution spectra is often challenging for directly imaged companions due to their faint magnitudes and close separations from their host stars. However, the Keck Planet Imager and Characterizer (KPIC; Delorme et al. 2021) is an instrument designed for this task. KPIC is a series of upgrades to the Keck II Telescope’s AO system and the NIRSPEC spectrograph, which includes a single-mode fiber injection unit coupled to the latter (e.g., McLean et al. 2000; Martin et al. 2018; López et al. 2020), allowing for the high-resolution spectroscopy ($R \sim 35,000$) of directly imaged companions in the K band (Wang et al. 2021, 2022; Xuan et al. 2022, 2024).

1.1. Atmospheric Abundances

The C/O ratio has been considered as a diagnostic of formation pathways for companions. If the companion went through a binary star formation process or protostellar disk instability process, it should present elemental abundances similar to that of the host star (Helled & Schubert 2009). For core or pebble accretion scenarios, however, the planet’s assembly can generate a variety of C/O ratios, mostly dependent on the planet’s location during its forming stage compared to the snow lines of volatile species such as CO, CO₂, and H₂O (Öberg et al. 2011). Most recently, Hoch et al. (2023) assessed the C/O ratio as a formation tracer for several companions and found that some observed C/O ratio trends cannot be fully explained by planet formation models in simulations. They conclude that measuring the C/O ratio for a companion is a useful proxy for trends in companion formation pathways, but it is not an assertive value that completely constrains formation mechanisms in individual objects. Therefore, measuring the C/O ratio using high-resolution spectroscopy can potentially inform companion formation trends, but may need to be considered in conjunction with other formation indicators.

Metallicity measurements may also be a useful proxy for the formation of companions. The metallicity, [Fe/H], of a companion is most likely enhanced compared to its host star if it presents a planet-like formation (e.g., core or pebble accretion; Helled & Schubert 2009), while metal enrichment is not expected if the companion formed from disk instability or disk fragmentation (e.g., Boss 2010). Beyond the formation information obtained from this parameter, the metallicity is also useful for informing potential membership of specific objects with a cluster (e.g., Perryman et al. 1998), where objects in the same cluster often present similar metallicity values due to their shared formation history.

1.2. Rotational Velocity

The rotational velocity can help constrain the angular momentum history of an object (e.g., Bryan et al. 2020, 2021). Rotation rates of stars have been used to trace stellar activity (e.g., Browning 2008). For low-mass stars and brown dwarfs, specifically, it appears that these objects are common rapid rotators, with a dependence on the object’s temperature, age, and mass (e.g., Mohanty & Basri 2003; Zapatero Osorio et al. 2006; Reiners & Basri 2008; Konopacky et al. 2012;

Snellen et al. 2014; Bryan et al. 2020; Hsu et al. 2021b; Tannock et al. 2021; Wang et al. 2021; Zendel et al. 2023; Landman et al. 2024, Hsu et al. 2024). For younger objects (≈ 10 –100 Myr), the rapid rotation can be explained by the gravitational contraction of these objects, which causes them to spin up as they age due to the conservation of angular momentum. This contraction ends at ≈ 1 Gyr. The rotational velocity of these objects is also mass dependent (e.g., Herbst et al. 2007), with higher-mass stars presenting longer rotation periods than brown dwarfs and low-mass stars. Reiners & Basri (2008) found that lower-mass stars and brown dwarfs tend to rotate faster because angular momentum loss mechanisms, such as magnetic braking, have longer timescales at lower mass and are therefore more inefficient at slowing down the object’s spin. These authors, therefore, find that young, low-mass objects initially have intermediate rotation rates and accelerate due to contraction in the first few 10 Myr. After this timescale, the objects with $M > 0.09 M_{\odot}$ begin to decelerate until they lose most of their angular momentum at tens of megayears. For low-mass objects with $M < 0.09 M_{\odot}$, the braking law becomes so weak that even at older ages the objects spin faster.

High-resolution spectroscopy allows for the measurement of spin, or $v \sin(i)$, of a target. Eliminating the $\sin(i)$ degeneracy that would allow for a true rotational velocity measurement requires photometrically derived rotational periods (e.g., Bowler et al. 2023). Several systems have been found to have their primary and secondary rotation axes misaligned from the orbital plane (e.g., Bryan et al. 2020, 2021; Bowler et al. 2023), which could be the consequence of a variety of phenomena, such as formation in the protoplanetary disk (e.g., Epstein-Martin et al. 2022), nearby mass concentrations during the collapse of the cloud core (e.g., Tremaine 1991), or interactions with objects outside of the forming system (e.g., Anderson et al. 2017).

1.3. Orbital Parameters

Orbital characterization of a companion provides dynamical footprints of its formation history, including possible distinctions between planet formation processes, such as core accretion and protoplanetary disk instability, and binary star formation processes, such as protostellar disk fragmentation (e.g., Tokovinin & Moe 2020; Offner et al. 2023). One particularly important orbital parameter for tracing the formation history of an object is its orbital eccentricity (e.g., Kipping 2013; Bowler et al. 2020; Do Ó et al. 2023; Nagpal et al. 2023). In the theory of planet formation, companions that form via core or pebble accretion most likely present lower eccentricities (i.e., closer to circular orbits) due to the collision of particles in the protoplanetary disk, while formation via gravitational instability or binary star mechanisms may present higher eccentricities during formation (e.g., Mayer et al. 2004). Dynamical interactions after formation may also modify the initial eccentricities of planets, with the possibility of scattering planets to wide separations on high eccentricity orbits (e.g., Chatterjee et al. 2008; Veras et al. 2009).

Due to the large separations from the host stars and consequently long periods of these objects, orbit characterization using relative astrometry of the companion is often limited. Generally, orbit fits are carried out in a Bayesian framework, where a time series of relative astrometry coupled with uniform parameter priors generates posteriors on the orbital parameters of the companion. Poorly sampled data of these orbits coupled

with priors have been shown to have biases on the final parameters of the companion, in particular the eccentricity, which is an important dynamical tracer of these objects (Martinez et al. 2017). This undersampling coupled with biased posteriors led to the generation of new prior approaches for orbit fitting that aimed to mitigate these biases, such as observable-based priors (O’Neil et al. 2019). However, for any priors, a single astrometry point for an undersampled orbit can significantly change the posterior distributions of orbital parameters.

Adding third-dimensional information using relative radial-velocity data between the companion and primary star to an orbit fit allows for a more constraining orbital characterization (e.g., Schwarz et al. 2016; Ruffio et al. 2019; Do Ó et al. 2023; Xuan et al. 2024). In particular, the radial velocity generally provides better constraints on the orbital plane of a companion due to the elimination of degeneracies in the angle of ascending node (Ω) and the argument of periaxis angle (ω), as well as eccentricity–inclination degeneracies.

1.4. The 1RXS J034231.8+121622 System

The companion to the star 1RXS J034231.8+121622, or 2MASS J03423180+1216225, was initially a resolved companion candidate reported by Janson et al. (2012). The data obtained by their work did not allow for the candidate to be distinguished from a background object. The companion was later confirmed by Bowler et al. (2015a), who found that the object was physically bound to the primary. The primary is an M4 type star that has shown signs of youth due to its X-ray emission (Shkolnik et al. 2009). The companion was initially classified as an L0 dwarf by the discovery paper, with a mass range of $35 \pm 8 M_{\text{Jup}}$ using evolutionary models for the companion’s luminosity, the assumed system age of 60–300 Myr, and a system distance of 32.995 ± 0.0727 pc from Gaia DR2 (Gaia Collaboration et al. 2018). However, Kuzuhara et al. (2022) recently found that this system is most likely associated with the Hyades, which has a much older age. They find a mass of $76\text{--}83 M_{\text{Jup}}$ for the companion using this new age. This result prompts a recalculation of the primary mass and, consequently, the overall system mass.

In this work, we characterize the 1RXS J034231.8+121622 system. In order to better constrain the companion’s orbit, we use Keck/NIRC2 data to directly image and obtain a new astrometric data point and Keck/KPIC data to obtain radial velocities and characterize the atmosphere (effective temperature T_{eff} , surface gravity $\log(g)$, metallicity $[\text{Fe}/\text{H}]$, spin $v \sin(i)$, and C/O ratio) of the companion and the host star.

Using the information provided by high-resolution spectroscopy, we constrain the possible formation scenarios for this specific companion. This work is organized as follows. In Section 2, we present our data reduction to obtain the NIRC2 astrometry point (Section 2.1) and to reduce the KPIC spectrum (Section 2.2). Our results are presented in Section 3, with the temperature, $\log(g)$, and $[\text{Fe}/\text{H}]$ fits shown in Section 3.1. The new system mass is derived in Section 3.2, and the new orbital parameters are presented in Section 3.3. Section 3.4 presents the C/O ratio analysis (Section 3.4.1) and rotational velocities (Section 3.4.2) for both objects. We discuss and conclude our results in Sections 4 and 5, respectively.

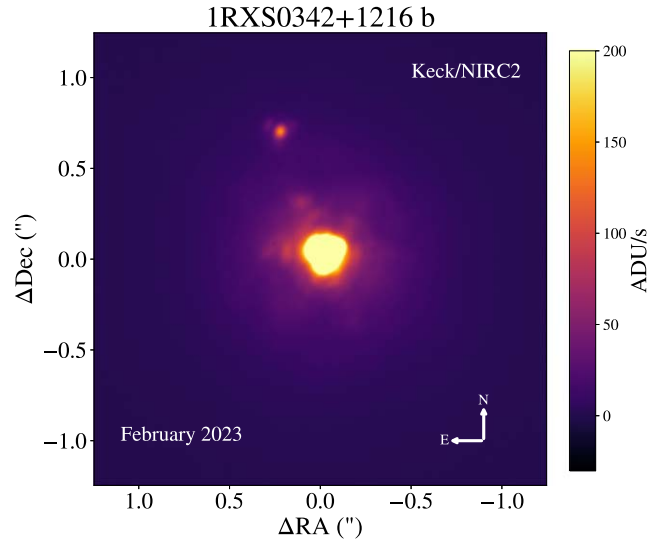


Figure 1. Final median combined image of the companion 1RXS0342+1216 b obtained with NIRC2 on Keck on 2023 February 8.

2. Methods

2.1. Keck/NIRC2 Data Reduction

We obtained astrometry for the 1RXS J034231.8+121622 system with the NIRC2 camera on the W. M. Keck Telescope II on UT 2023 February 8 using natural guide star adaptive optics with the primary as the guide star (Wizinowich 2013). This epoch of observation comes five years after the last published astrometry point from 2018 by Bowler et al. (2020). We take 30 exposures with an exposure time of 0.5 s and 120 coadds. Our images do not use a coronagraph as the target is at ≈ 700 mas from the host star with a contrast of 3.2×10^{-2} and is easily visible in the raw frames.

Our data reduction pipeline follows the prescription in Yelda et al. (2010). We perform background subtraction, flat-fielding, bad pixel correction, distortion correction using `Rain` (a Python adaptation of the distortion correction package `Drizzle` (Fruchter & Hook 2002) with the distortion solution from Service et al. 2016), subpixel shifting to align the centroid of the primary in all frames, and finally a derotation of the image. For the derotation of the image, we use the parameters:

$$\theta = \text{PARANG} + \text{ROTPOSN} - \text{INSTANGL} + \text{OFFSET} \quad (1)$$

where the `PARANG` variable is the parallactic angle, `ROTPOSN` is the rotator position angle, `INSTANGL` is the instrument angle for NIRC2, and the `OFFSET` variable is the position angle offset needed to align the images with celestial north, measured to be $0^\circ.262 \pm 0^\circ.018$ by Service et al. (2016). The final median combined image is shown in Figure 1. In order to obtain astrometry of the companion and the primary, we use the `StarFinder` algorithm (Diolaiti et al. 2000) for point-spread function centroiding. The astrometry is generated by centroiding the median of the images, while the uncertainties are determined by centroiding each individual image and then obtaining the standard deviation of the centroids. To convert from pixels to milliarcseconds, we use the plate scale provided by Service et al. (2016) of 9.971 ± 0.004 mas pixel $^{-1}$. The final obtained relative astrometry of the companion is presented in Table 1. Compared to previous astrometric data points from

Table 1
Relative Astrometry of 1RXS0342+1216 b

Epoch	Separation (mas)	Position Angle ($^{\circ}$)	Filter	Instrument	Reference
2007.951	883.0 ± 0.2	17.58 ± 0.09	Ks	Keck/NIRC2	Bowler et al. (2015b)
2008.63	860 ± 8	17.3 ± 0.4	i'	AstraLux Norte	Janson et al. (2012)
2008.87	866 ± 8	17.8 ± 0.4	i'	AstraLux Norte	Janson et al. (2012)
2010.659	851 ± 3	18.7 ± 0.1	H	Gemini-S/NICI	Bowler et al. (2015b)
2012.02	834 ± 57	17.6 ± 1.7	i'	AstraLux Sur	Janson et al. (2014)
2012.645	831 ± 2	18.71 ± 0.07	H	Keck/NIRC2	Bowler et al. (2015a)
2013.044	822 ± 8	19.1 ± 0.7	L'	Keck/NIRC2	Bowler et al. (2015a)
2018.08	772.3 ± 1.8	19.6 ± 0.1	Ks	Keck/NIRC2	Bowler et al. (2020)
2023.108	712.1 ± 0.4	20.82 ± 0.15	Ks	Keck/NIRC2	This Work

Janson et al. (2012, 2014), Bowler et al. (2015a, 2015b), and Bowler et al. (2020), the companion appears to be moving toward the host star with an increasing position angle.

2.2. Keck/KPIC Data Reduction and Spectral Modeling

KPIC data for the companion were obtained on UT 2020 September 28 and 2021 July 3. For both epochs, the observations were done in K band (1.9 – 2.4 μ m) and have an average spectral resolution of $R \sim 35,000$ (Delorme et al. 2021). The instrument presents a fiber injection unit with single-mode fibers that increase stellar light rejection and sky background (Echeverri et al. 2022). Our companion exposures for the 2020 epoch consisted of six exposures of 300 s each, with the companion in fiber 2, which presented the highest throughput after calibrations. We also obtained two host star exposures of 60 s each, with the host star present in fibers 1 and 2. For the 2021 epoch, we obtained five exposures of 300 s each for the companion, alternating between fiber 1 and fiber 2 to enable nod subtraction. The purpose of nodding, which is a strategy first implemented in 2021, is to reduce background noise, since the background taken during daytime calibrations may not match the nighttime background. It is most useful for faint targets, so it does not significantly affect this target's signal-to-noise ratio (S/N) since it is fairly low contrast. We also obtained two exposures of the host star on fibers 1 and 2, with 60 s exposure for each, and exposures for an A0 star (HIP 16322) for telluric calibration. The data were reduced using the KPIC pipeline (Wang et al. 2021).¹⁵ The reduction includes subtraction of adjacent frames for thermal background, bad pixel correction, and wavelength calibration using data from the telluric star to fit the trace of the four fibers and nine orders. After this initial data reduction, we used the Python package `bread` to analyze this data set.¹⁶ `bread` follows the formalism of Ruffio et al. (2019), which uses a spline forward-modeling methodology (Ruffio et al. 2023). The main challenge of high-resolution spectroscopy is in the S/N, where individual spectral lines present low S/N. In this method, the data are considered a sum of a model and a noise quantity:

$$\mathbf{d} = \mathbf{M}_{\text{RV}} \phi + \mathbf{n} \quad (2)$$

where the data vector d is composed of a model M_{RV} combined with linear parameters ϕ and the noise vector n . The forward model relies on maximum likelihood estimation of the companion's signal by jointly fitting the companion data and

the host starlight from models for each of the components (Agrawal 2022). This way, the fit can account for starlight contamination at the companion's location. For the companion, the host star, and the A0 telluric calibration star, we employed PHOENIX ACES AGSS COND models (Husser et al. 2013) as the forward model template. Unfortunately, the data from the 2021 epoch had poor throughput and therefore highly uncertain results in the atmospheric analysis of the companion and the host star due to poor observing conditions. For that reason, that epoch was not used for our analysis, and we used only KPIC data from 2020, which had a throughput of 1.4%–1.8%, depending on the fiber.

KPIC/NIRSPEC possesses nine spectral orders in the K band for each object. For this analysis, we only use orders 33 (2.29–2.34 μ m) and 32 (2.36–2.41 μ m), due to the high S/N and well-modeled telluric lines in these orders (Ruffio et al. 2023). Our algorithm follows a Markov Chain Monte Carlo approach (Foreman-Mackey et al. 2013), and for all of our fits we use 512 walkers with 10,000 burn-in steps and 10,000 steps.

3. Results

3.1. Temperature, $\log(g)$, and $[\text{Fe}/\text{H}]$

Using the `bread` package, we first use the Keck/KPIC data to obtain atmospheric parameters for both the companion and the host star. Our PHOENIX grids were used to fit for temperature, $\log(g)$, metallicity ($[\text{Fe}/\text{H}]$), spin, and radial velocity.

Our final corner plots are presented in Figure 2. We obtain a temperature of 2510_{-40}^{+40} K and a $\log(g)$ of $5.36_{-0.14}^{+0.10}$ (68th percentile) for the companion and a temperature of 3460_{-10}^{+10} K and a $\log(g)$ of $4.94_{-0.06}^{+0.04}$ for the host star. We note that the $\log(g)$ values for both objects are close to the grid ceiling of 5.5 for the companion grid and 5.0 for the primary grid. The reason for these upper bounds is to keep the limit of $\log(g)$ in agreement with interior structure models, which we incorporate by considering the evolutionary models from Baraffe et al. (2015). For any age in these models, values above $\log(g) = 5.5$ are inconsistent with the physical predictions. Surface gravity values that reach the grid ceiling have been reported by other works that use high-resolution spectroscopy for isolated low-mass stars and brown dwarfs (e.g., Del Burgo et al. 2009; Hsu et al. 2021a; Hsu et al. 2024), so this is a known model issue in atmosphere fitting to high-resolution data. Other works have kept $\log(g)$ fixed in order to avoid this issue (e.g., Blake et al. 2010; Theissen et al. 2022). Bowler et al. (2015a) obtained moderate-resolution ($R \sim 4000$) spectra of the companion

¹⁵ https://github.com/kpicteam/kpic_pipeline

¹⁶ <https://github.com/jruffio/bread>

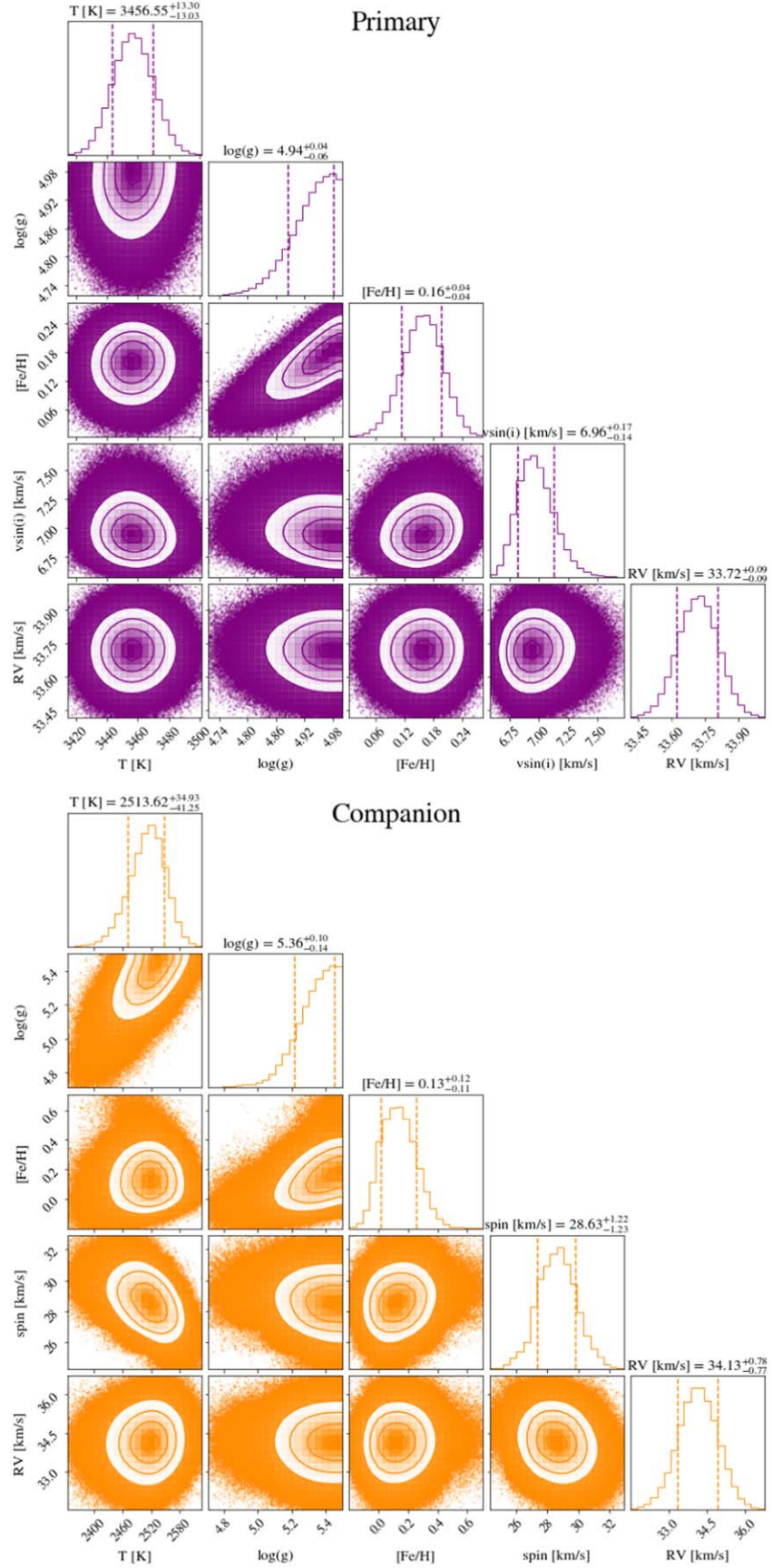


Figure 2. Corner plots showing the posteriors for temperature, $\log(g)$, $[\text{Fe}/\text{H}]$, $\text{vsin}(i)$, and RV for the primary and companion using KPIC data from 2020.

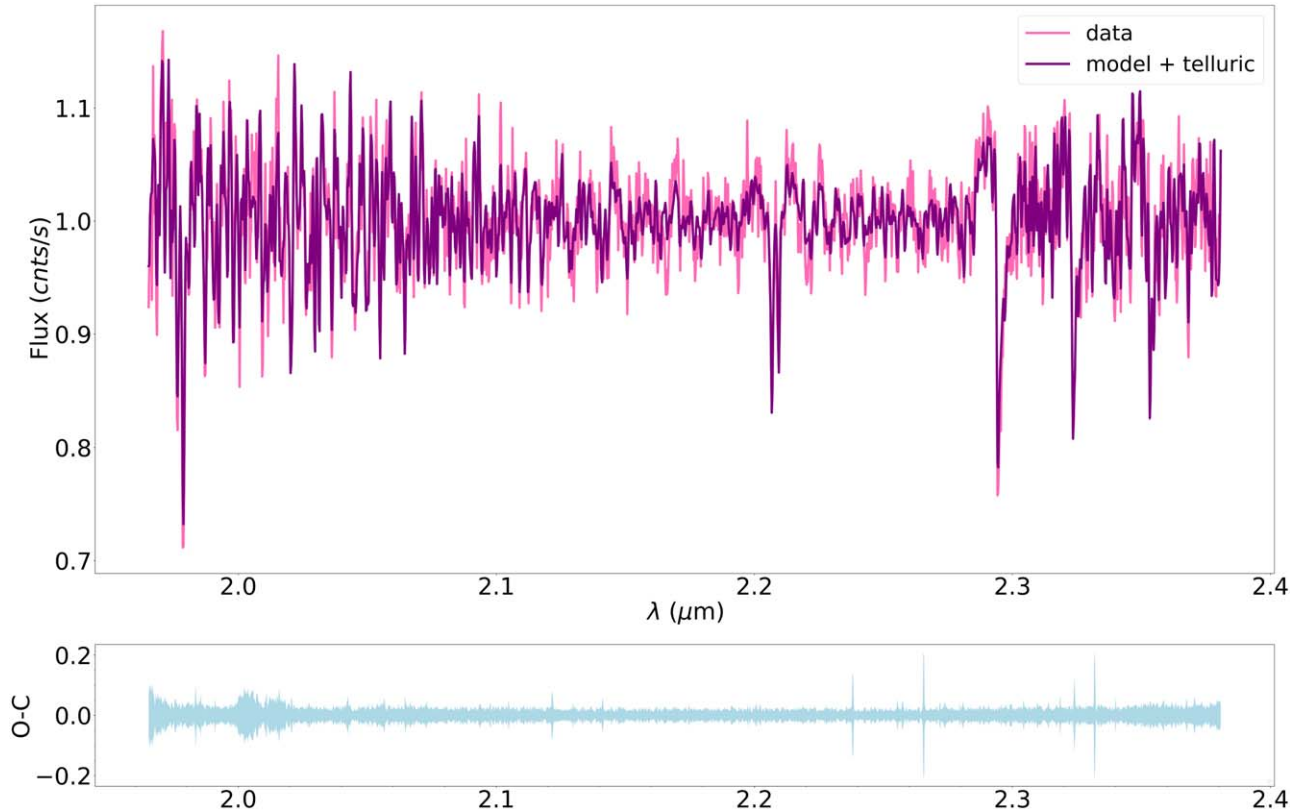


Figure 3. Final fit for the moderate-resolution spectrum from OSIRIS. The temperature fit is 2760 ± 12 K, $\log(g)$ is 5.2 ± 0.04 . This pair of parameters yields a mass of $0.09 \pm 0.02 M_{\odot}$ for the companion, slightly above but still consistent with the KPIC fit.

using OSIRIS on Keck (0.365–1.05 μm). In order to validate our atmospheric fits with KPIC data, we also fit the OSIRIS spectra using the same model grid. We fit for the temperature, $\log(g)$, and RV using the forward-modeling routine Spectral Modeling Analysis and RV Tool (SMART; Hsu et al. 2021a, 2021b) using PHOENIX COND models. We obtain a temperature of 2760 ± 12 K and a $\log(g)$ of 5.2 ± 0.04 (68th percentile) with that data set. The temperature of the companion is not consistent with the KPIC result (about 200 K higher), while the OSIRIS result yields a similar $\log(g)$ value. In this case, we fit for the data with the continuum subtracted from the spectrum. We present the OSIRIS best fit for the data in Figure 3. We also plot our KPIC spectra compared to the models in Figures 4 and 5.

The formal statistical uncertainties from model fits for the atmospheric parameters are underestimated as they do not account for any systematic uncertainties in the models themselves or errors in interpolation of the grid between steps. In order to take this underestimation into account, we inflate our uncertainties in temperature to ± 50 K and in $\log(g)$ to ± 0.3 for both the companion and the host star, which corresponds to half of the model grid spacing size of 100 K for effective temperature and 0.5 for $\log(g)$. This uncertainty value is in accordance with our previous works that accounted for the underestimation in model uncertainties due to the systematics in grid interpolation (e.g., Konopacky et al. 2013; Wilcomb et al. 2020; Ruffio et al. 2021; Hoch et al. 2022).

3.2. System Mass Derivation

For this system, Bowler et al. (2015b) report a primary mass of $0.20 \pm 0.05 M_{\odot}$, a companion mass of $35 \pm 8 M_{\text{Jup}}$, and,

therefore, a total system mass of $0.23 \pm 0.05 M_{\odot}$. These masses were found by interpolating luminosity values with evolutionary models from Baraffe et al. (1998) for the system's age of 60–300 Myr. However, Kuzuhara et al. (2022) found using new Gaia data that this system is associated with the Hyades (membership probability $> 99.9\%$), which presents a much older age of 750 ± 100 Myr (Brandt & Huang 2015). This older age estimate necessitates a recalculation of the mass of the primary and the companion in order to determine the total system mass.

In order to estimate the mass of the system given this new age estimate, we interpolate our newly derived effective temperature (T_{eff}) and $\log(g)$ chain pairs given by our KPIC 2020 data (see Figure 2 for corner plots) with evolutionary models provided by Baraffe et al. (2015), randomly sampling from the Hyades age estimate range in a Monte Carlo fashion to obtain a range of possible masses for the primary, secondary, and the entire system.

We obtain a median host star mass of $0.30 \pm 0.15 M_{\odot}$ and a median companion mass of $0.08 \pm 0.01 M_{\odot}$ (68th percentile). This sums to a total system mass of $0.38 \pm 0.15 M_{\odot}$. When we only include the effective temperature in our interpolation, we obtain masses that are consistent with the fit where $\log(g)$ is included ($0.41 \pm 0.15 M_{\odot}$ total system mass, with a primary mass of $0.33 \pm 0.15 M_{\odot}$ and secondary mass of $0.08 \pm 0.01 M_{\odot}$). Updating both the temperature and age of the components therefore yields higher masses. Our resulting mass for the companion places it near or slightly above the hydrogen-burning limit ($\sim 0.072 M_{\odot}$; Burrows et al. 2001), consistent with Kuzuhara et al. (2022), who found $76\text{--}83 M_{\text{Jup}}$ using the companion's luminosity. We also fit for the mass of the companion using the temperature and $\log(g)$ pairs from the

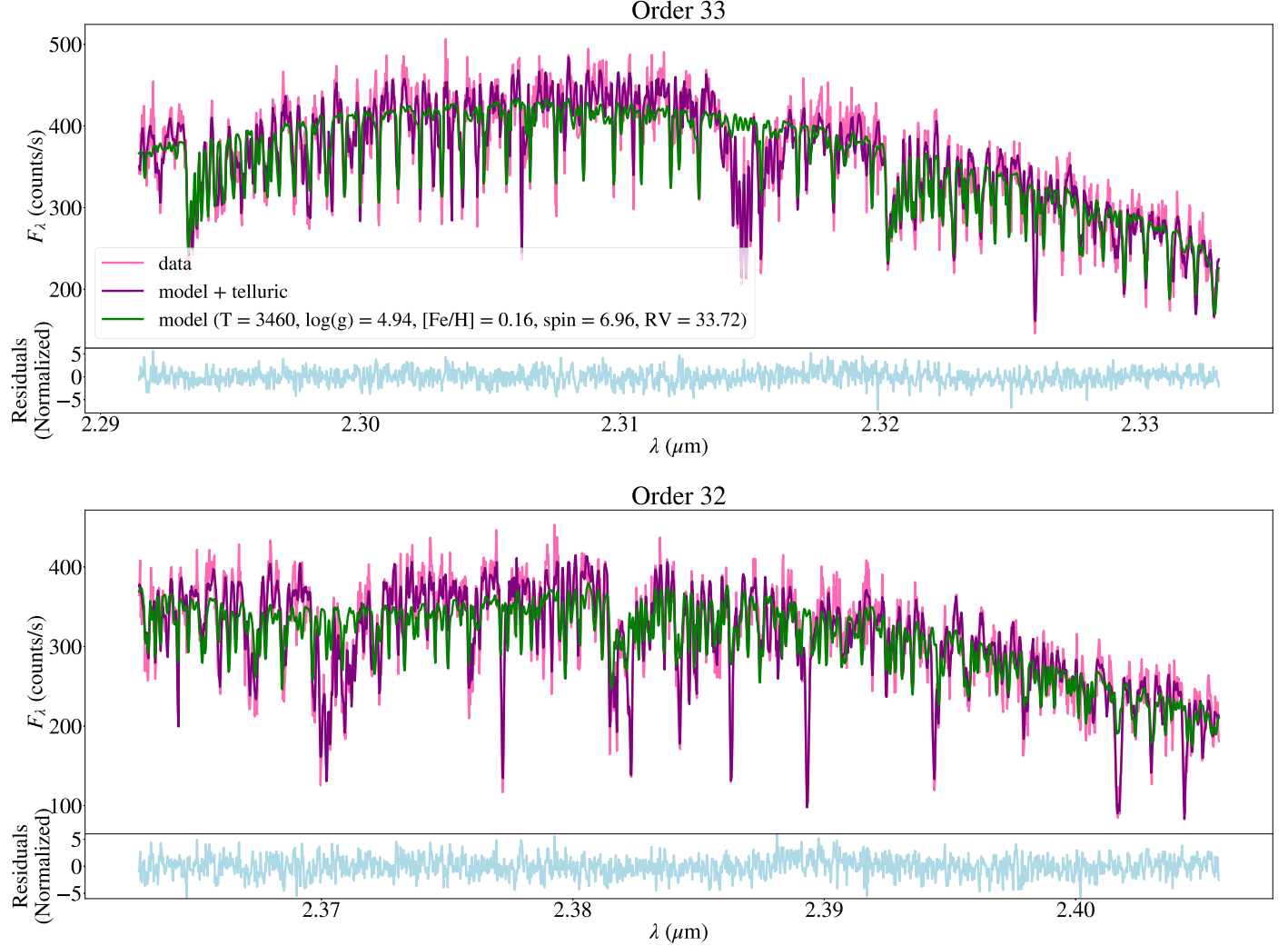


Figure 4. KPIC spectrum for the primary star compared to the best-fit models from `bread`s. The pink curve shows the data, with the green curve representing the atmospheric model and the purple curve representing the atmospheric model + telluric model. The blue curve in the lower panel shows the residuals, which are normalized by the data before uncertainty inflation.

OSIRIS best fit. We obtain a slightly higher, but still consistent, result of $0.09 \pm 0.02 M_{\odot}$ for the companion.

3.3. Orbital Characterization with New Data

We use the new 2023 astrometry epoch to fit for the orbit of the companion. The most recent orbit fit of the companion was done by Do Ó et al. (2023) using observable-based priors, which have been shown to decrease biases in undersampled orbits done with direct imaging. The purpose of observable-based priors is to improve orbital estimates for orbits where the data cover a low percentage of the orbital arc (<40%).

We briefly summarize the formulation of observable-based priors. A detailed formulation is outlined in O’Neil et al. (2019). Observable-based priors assume that all regions of observable parameter space that can be observed are equally likely, emphasizing uniformity in observables rather than in model parameters (such as eccentricity and periastron passage epoch). Our orbit fit starts with measured observables from the astrometry, $x(t)$, $y(t)$, and $v_z(t)$, where x and y are the object’s positions (R.A. and declination) in the plane of the sky relative to the position of the primary (x_o and y_o) and v_z is the velocity relative to the star. These measured observables are linearly

related to the orbital observables (which describe the position and motion in the orbital plane) by the Thiele–Innes constants (e.g., Hartkopf et al. 1989; Wright & Howard 2009). Due to this linear relationship, a uniform distribution in the measured observables would imply a uniform distribution in the orbital observables. The orbital observables, denoted here as X , Y , V_x , and V_y , are also connected to the model parameters according to the following equations (e.g., Hilditch 2001; Ghez et al. 2003):

$$X = a(\cos E - e) \quad (3)$$

$$Y = a(\sqrt{1 - e^2} \sin E) \quad (4)$$

$$V_x = -\frac{\sin E}{1 - e \cos E} \sqrt{\frac{GM}{a}} \quad (5)$$

$$V_y = \frac{\sqrt{1 - e^2} \cos E}{1 - e \cos E} \sqrt{\frac{GM}{a}} \quad (6)$$

where G is the gravitational constant, E is the eccentric anomaly, e is the eccentricity, a is the semimajor axis, and M is the mass of the system. By transforming between measured observables and orbital observables, and then between orbital observables and model parameters, we can transform between measured

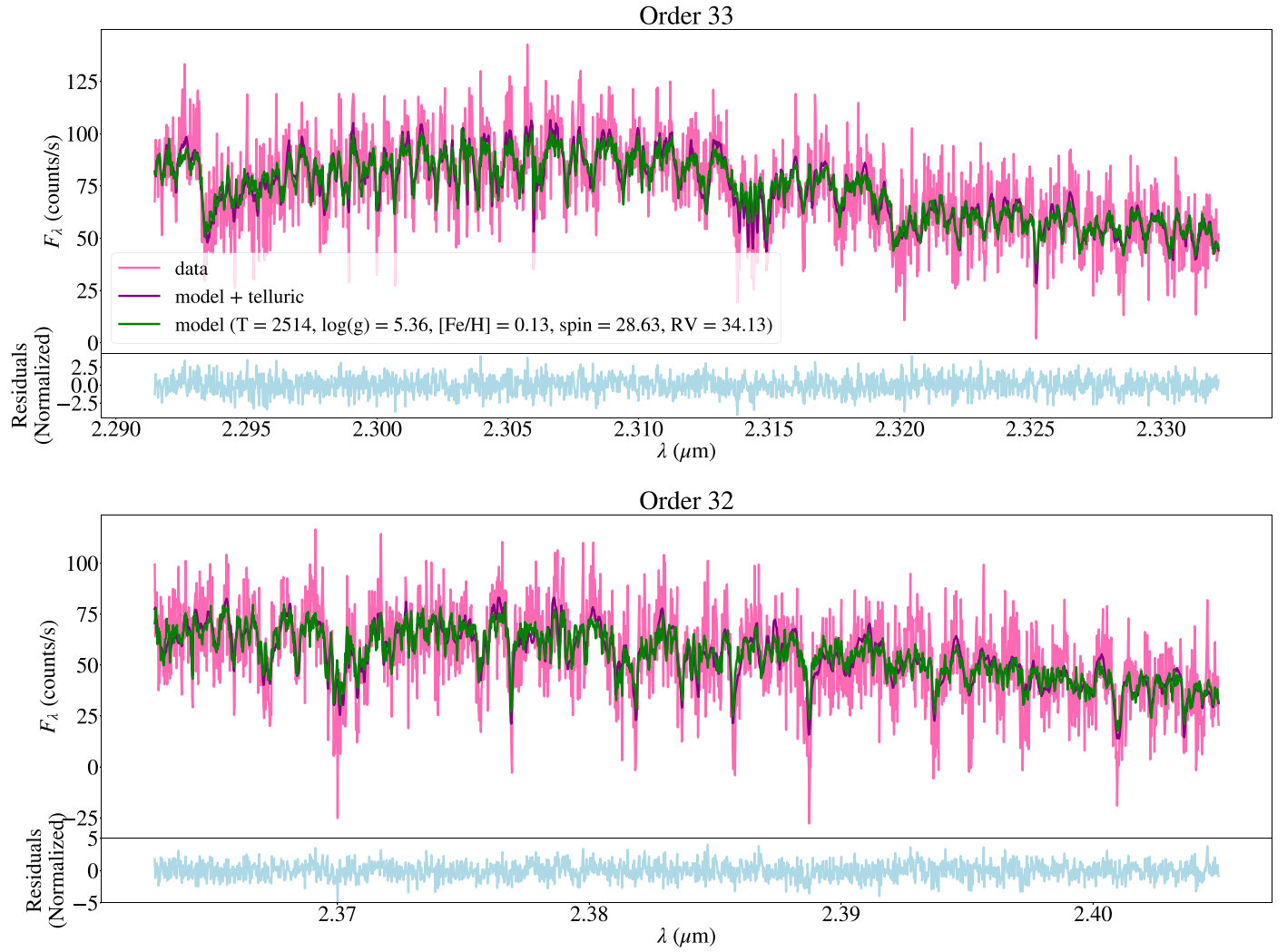


Figure 5. Same as Figure 4, but for the companion.

observables and model parameters. This allows us to express a distribution that is uniform in the measured observables in terms of model parameters. Traditional uniform priors in orbital parameter space lead to a biased region in periastron passage (T_o), where the T_o tends to artificially coincide with the observation epochs (Konopacky et al. 2016). This bias is mitigated in observable-based priors because they suppress this biased region of the parameter space when sampling it.

Here, we revisit the analysis done in Do Ó et al. (2023) by fitting for the companion's orbital parameters with observable-based priors. We use the software Efit5 (Meyer et al. 2012). Efit5 uses MULTINEST (Feroz & Hobson 2008; Feroz et al. 2009), a multimodal (or nested) sampling algorithm, to perform a Bayesian analysis on the data. For all of these fits, we use 3000 live points in the nested sampling algorithm.

Because orbit fits for directly imaged companions often rely on fixed total system masses to derive constraining posteriors when dynamical masses are not employed, we investigate how much the updated mass affects the original orbit fit for 1RXS0342+1216 b by running the fit for both the old mass estimate ($0.23 M_{\odot}$) and new mass estimate ($0.38 M_{\odot}$). Since our interest in these first fits is only to see how the new mass affects the resulting orbital parameters, we include no new astrometry or RVs, and use only relative astrometry up to 2018

(see Table 1). We use the distance estimate of 32.995 ± 0.0727 pc from Gaia DR2 (Gaia Collaboration et al. 2018; as was done previously in Bowler et al. 2020 and Do Ó et al. 2023).

Our orbit fit results are presented in Figure 6. The orbit fit with the new mass estimate for the system significantly changes the orbital parameter posteriors. In particular, the eccentricity of the companion changes from $0.90_{-0.48}^{+0.0}$ to $0.35_{-0.11}^{+0.25}$, a much lower estimate. This change is coupled with a significant change in periastron passage, with the new mass estimate having a wider spread of possible periastron passage epochs and placing it further away from current observation epochs. The inclination of the companion also changed from 65_{-40}^{+10} ° to 82_{-1}^{+1} °, moving from a highly uncertain orbit orientation to an orientation where the orbit is close to edge-on. We show a visual example of these two orbit fits in Figure 7. We also verify that a similar change in the eccentricity tail occurs with uniform parameter priors rather than with observable priors. Our results for uniform priors are presented in Appendix B.

For all of our orbit fits with new data, we use an updated system distance of $32.96_{-0.024}^{+0.022}$ pc from Bailer-Jones et al. (2021). We first fit for the orbit of 1RXS0342+1216 b using only the new astrometry epoch from 2023 obtained with Keck/NIRC2 and presented in Table 1. We find that the fit yields a period of 310_{-40}^{+40} yr, with an eccentricity of $0.45_{-0.16}^{+0.14}$. The last

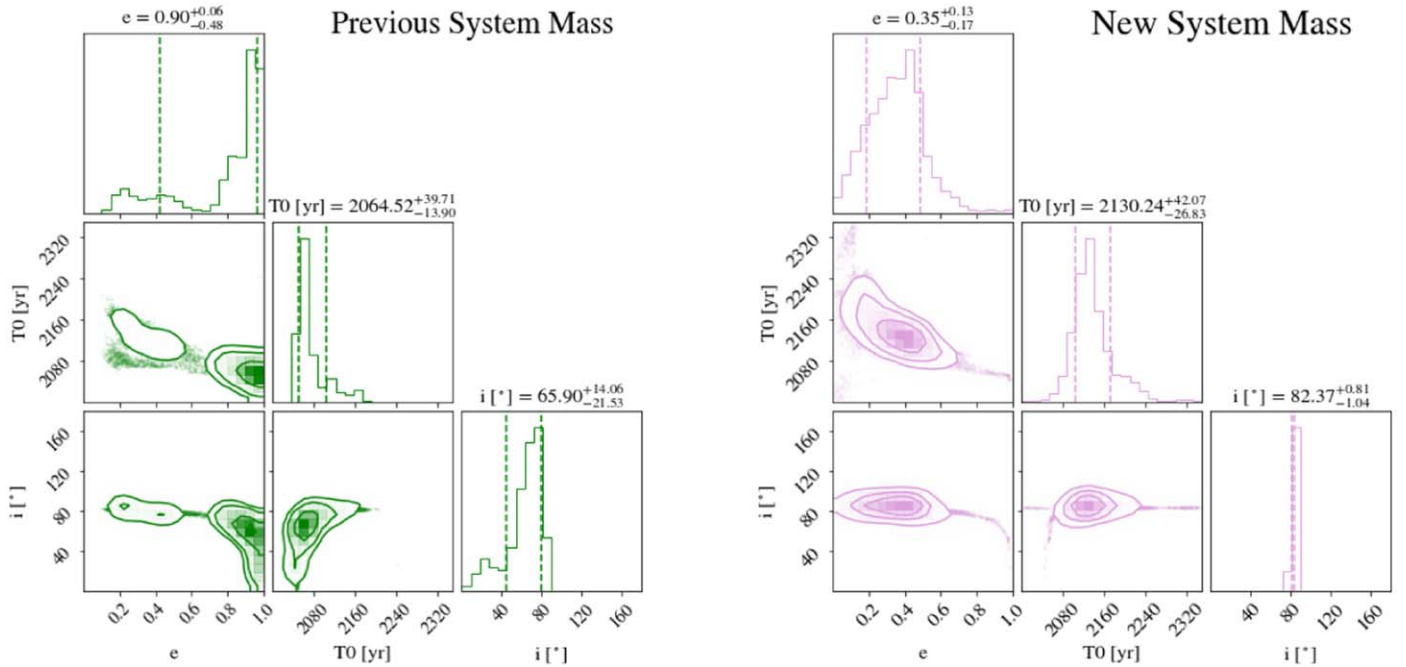


Figure 6. Corner plots for 1RXS0342+1216 b's orbital parameters with the previous system mass of $0.23 M_{\odot}$ (left) and new system mass of $0.38 M_{\odot}$ (right). No new astrometry or radial-velocity data were included in this orbit fit. Full corner plots can be found in Appendix A.

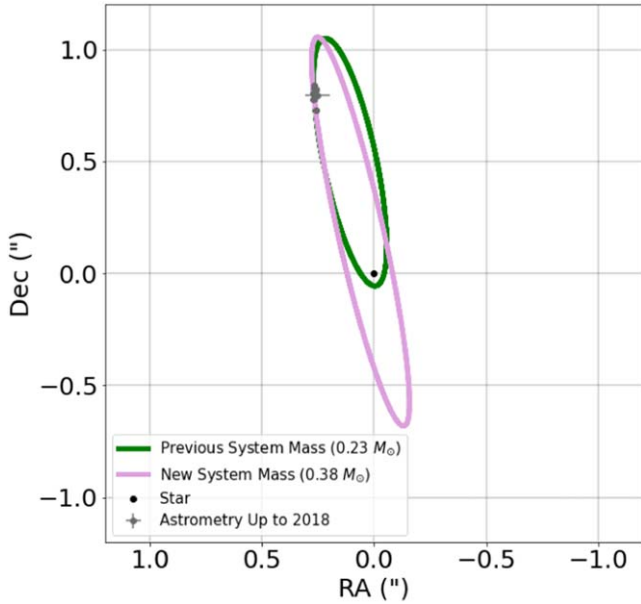


Figure 7. Visual orbit fit for the companion with the previous and new system mass. No additional astrometry or RV data were used in these fits.

astrometric data point before the one presented in this work is from five years earlier, in 2018. We then fit for the orbit of the companion using only the relative radial-velocity data from KPIC's 2020 data set. The radial velocities of the host star and the companion, and the relative radial velocity are presented in Table 2. From the measurement, the relative radial velocity of the companion is practically zero ($0.41 \pm 0.78 \text{ km s}^{-1}$). This signifies that the companion is not significantly moving toward or away from our line of sight at its current orbital phase, meaning that the degeneracy on the orbital plane remains mostly unconstrained (in particular the Ω and ω 180° degeneracy). Both of these resulting fits (new astrometry only and new RV only) can be found in Appendix A.

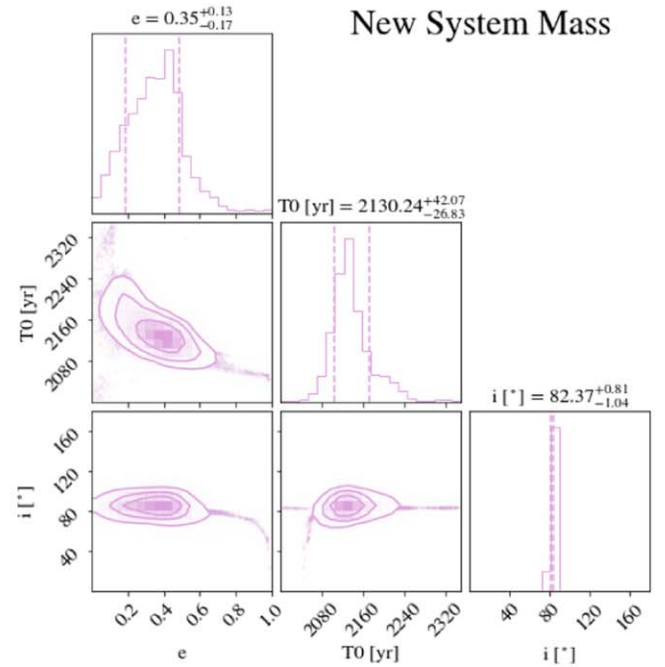


Table 2
Relative Radial Velocity of 1RXS0342+1216 b

Epoch	Host Star RV (km s ⁻¹)	Companion RV (km s ⁻¹)	Relative RV (km s ⁻¹)	Instrument
2020.742	33.72 ± 0.09	34.13 ± 0.77	0.41 ± 0.78	KPIC

Finally, we fit for the companion's orbit with the new total system mass, new astrometry epoch, and the RV obtained with KPIC. Here, we use both data types to maximize the amount of information given to the orbit fit. Our final orbit fit is presented in Figure 8. We find that the companion's new orbit fit has a well-constrained inclination of $83.13^\circ_{-2.20^\circ}$, placing it in a nearly edge-on orbit. The eccentricity of the companion is $0.41^{+0.27}_{-0.08}$, favoring moderate eccentricity solutions and disfavoring circular (<0.2) and highly eccentric (>0.9) orbital solutions. The periastron passage of the companion is found to happen in $2165.17^{+45.30}_{-59.06}$ yr. This is about 150 yr away from current observations. We plot 100 randomly sampled visual orbits and separation/position angles as a function of time in Figure 9.

We also fit for the final orbit of the companion with the traditionally used uniform priors on the orbital parameters. The purpose of this exercise is to verify that both observable and uniform prior fits give similar orbital parameter posteriors. All of our uniform prior results are shown in Appendix B.

The orbital posteriors for the different data and mass configurations are found in Table 3.

3.4. Derivation of Atmospheric Parameters

3.4.1. Fitting C/O Ratio

In order to explore the C/O ratio of the companion, we generated a custom grid of PHOENIX models in which the abundances of carbon and oxygen were selected according to the predictions of Öberg et al. (2011), as described in

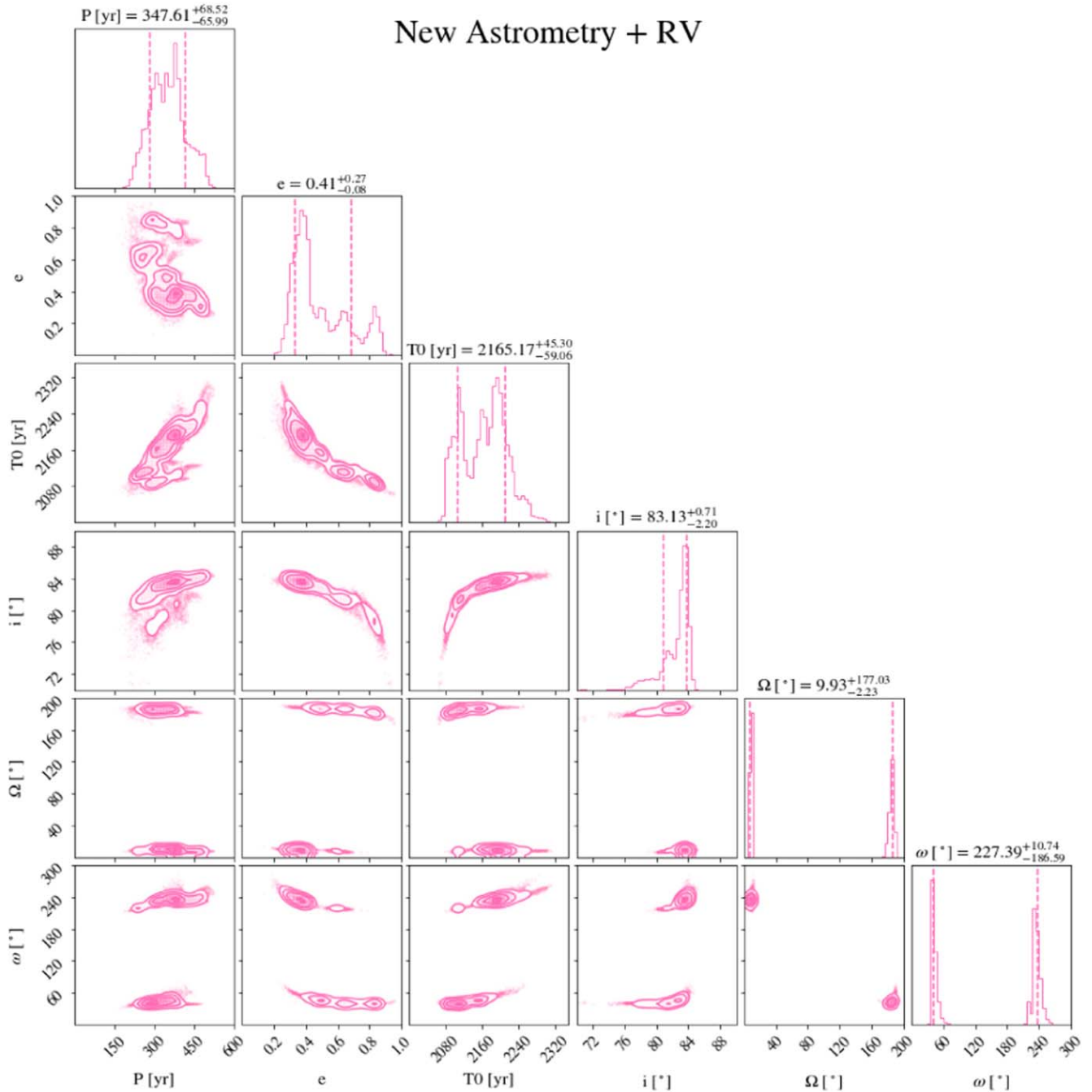


Figure 8. New orbit fit of 1RXS0342+1216 with the new 2023A astrometry epoch and 2020 RV data point.

Konopacky et al. (2013). Briefly, Öberg et al. (2011) predict specific absolute abundances of C and O in the gas phase based on their model as a function of the ratio of solid to gas accretion in the atmosphere, which results in C/O between 0.45 and 1. The purpose of selecting specific values from this model was to generate a grid based on real predictions from physical models, and to explore the likely values of C/O based on those models. However, we interpolate between the models in the grid and therefore can explore any intermediate values of C/O. We generated grids for both the host star and the companion in order to be able to compare the two. In our custom model grids, we hold the temperature, $\log(g)$, and metallicity constant at the best-fit values found in Section 3.1 for the host star and the companion. Previous work has explored fitting the temperature

and $\log(g)$ together with the C/O ratio in moderate-resolution data (Konopacky et al. 2013). They find that fitting the temperature and $\log(g)$ simultaneously with C/O does not significantly affect the posteriors for C/O, but does require a significantly larger computational expense. For that reason, we do not fit for these parameters at the same time and instead fix temperature and $\log(g)$ when fitting for C/O. The grids are incorporated into the breads framework for fitting.

The spacing in the C and O grid from Öberg et al. (2011) is not free but rather physically motivated—i.e., it is derived from gas and grain abundances of C- and O-containing species (e.g., CO_2 , CO, and H_2O) and is parameterized over stellar abundances (from Figure 3 in Öberg et al. 2011). Since we are performing a forward model rather than a free retrieval,

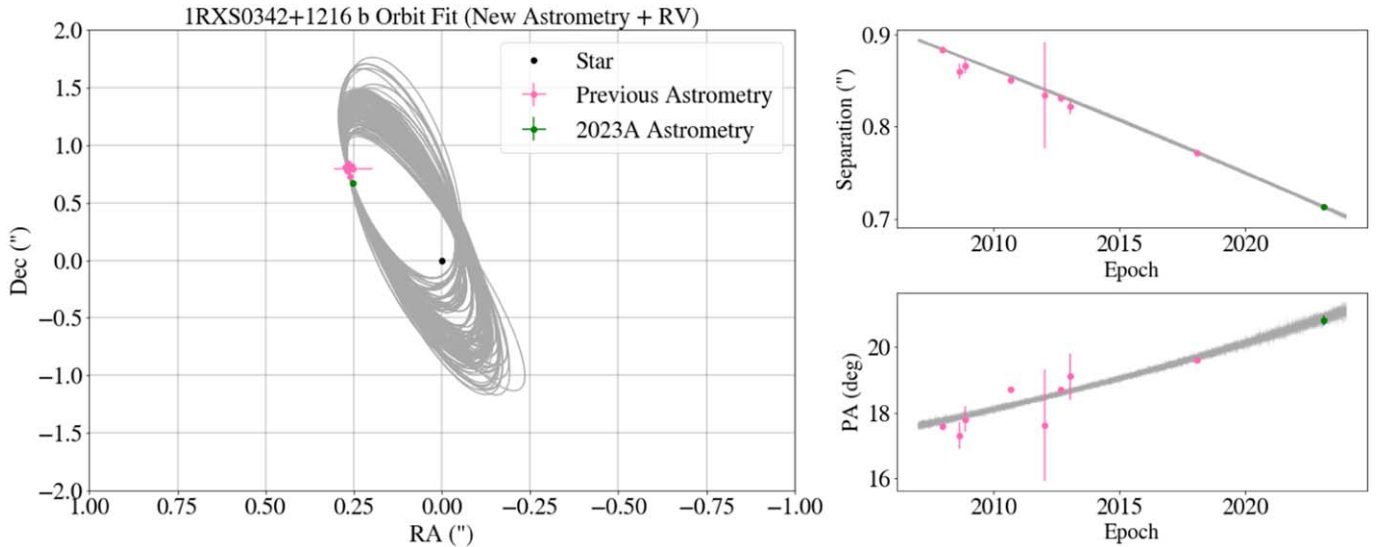


Figure 9. New orbit fit of 1RXS0342+1216 with the new 2023A astrometry epoch, the 2020 RV data point, and the updated total system mass. The left panel shows in gray 100 randomly sampled visual orbits from the posteriors with the current astrometry plotted on top (previous astrometry points are shown in pink while the 2023A astrometry point is shown in green). The top-right plot shows in gray 100 randomly sampled orbits' separation in arcseconds from the host star as a function of epoch. The bottom-right plot is the same as the top right, but with the position angle, or P.A., in degrees as a function of epoch.

Table 3
Orbit Fit for 1RXS0342+1216 b

Configuration	Period (yr)	Eccentricity	T_0 (yr)	Inclination ($^{\circ}$)	Ω ($^{\circ}$)	ω ($^{\circ}$)
Astrometry up to 2018, System Mass of $0.23 M_{\odot}$	$219.30^{+94.15}_{-48.96}$	$0.90^{+0.07}_{-0.40}$	$2057.69^{+29.11}_{-58.58}$	$64.99^{+14.10}_{-39.28}$	$180.98^{+13.69}_{-157.25}$	$91.33^{+157.40}_{-73.51}$
Astrometry up to 2018, System Mass of $0.38 M_{\odot}$	$255.85^{+46.26}_{-36.60}$	$0.35^{+0.13}_{-0.17}$	$2130.24^{+42.07}_{-26.83}$	$82.37^{+0.81}_{-1.04}$	$13.04^{+178.19}_{-2.88}$	$213.00^{+19.12}_{-178.87}$
Astrometry up to 2023, System Mass of $0.38 M_{\odot}$	$311.44^{+43.04}_{-44.70}$	$0.45^{+0.14}_{-0.16}$	$2149.27^{+49.02}_{-28.82}$	$82.84^{+0.80}_{-0.99}$	$186.11^{+3.74}_{-178.36}$	$80.31^{+146.80}_{-35.89}$
Astrometry up to 2018 + RV, System Mass of $0.38 M_{\odot}$	$253.72^{+72.21}_{-55.22}$	$0.49^{+0.21}_{-0.13}$	$2118.59^{+49.22}_{-34.03}$	$81.78^{+1.25}_{-2.49}$	$9.31^{+118.40}_{-1.73}$	$218.50^{+11.41}_{-73.72}$
Astrometry up to 2023 + RV, System Mass of $0.38 M_{\odot}$	$347.61^{+68.52}_{-65.99}$	$0.41^{+0.27}_{-0.08}$	$2165.17^{+45.30}_{-59.06}$	$83.13^{+0.71}_{-2.20}$	$9.93^{+177.03}_{-2.23}$	$227.39^{+10.74}_{-186.59}$

these values must be chosen in advance. We chose the models presented by Öberg et al. (2011) because they are consistent with the expectations of C and O values for directly imaged objects and because the calculation is more computationally efficient when an already existing grid of C and O abundances is used. When we fit for the C/O ratio for the primary, we find that the C/O values are closer to the lower boundary of the grid, indicating that its true C/O value is below 0.45. In order to remain consistent with their physical predictions, we incorporate lower C/O ratio values into the grid (down to the value of 0.25) by using a spline interpolation method to extend the C and O abundances derived in their work to lower values of C/O. With this extended grid, the resulting C/O ratios for the host star and companion are 0.416 ± 0.007 and 0.55 ± 0.02 , respectively (see Figure 10). The companion's C/O is broadly consistent with the solar value of ≈ 0.59 (Asplund et al. 2021), while the primary has subsolar C/O. The best-fit C/O values yield small statistical error bars and slightly different, but still consistent, spin/RV values than what was previously found using the PHOENIX model grid in Section 3.1. We note here that the C/O uncertainty values presented in the corner plots are not true uncertainties in the parameters, but rather statistical error bars due to the interpolation on the model grid. This interpolation generates systematic errors that do not reflect the true uncertainty of the C/O ratio for the object. Therefore, it appears that there are unaccounted-for uncertainties in the data that are not fully covered by the models. For this reason, we estimate that the C/O ratio found here is likely underestimating

the measurement uncertainties, which are likely closer to 0.1 (e.g., Hoch et al. 2023).

3.4.2. Rotational Velocities

Our obtained $v \sin(i)$ measurements are $6.96^{+0.17}_{-0.14}$ km s $^{-1}$ and $28.63^{+1.22}_{-1.23}$ km s $^{-1}$ for the primary and secondary, respectively. The upgraded NIRSPEC has $R \sim 35,000$ (compared to the $R \sim 25,000$ for the original NIRSPEC), which has an extrapolated minimum $v \sin(i)$ floor of 6.5 km s $^{-1}$, compared to 9 km s $^{-1}$ for the original NIRSPEC (Blake et al. 2010; Hsu et al. 2021a). The detection floor calculation for KPIC will be illustrated in an upcoming survey paper. The obtained $v \sin(i)$ measurement for the host star is close to the noise floor of the NIRSPEC instrument. For that reason, we conservatively adopt the noise floor of 9 km s $^{-1}$ for NIRSPEC as an upper limit on the primary's spin for our assessment of rotation rates (i.e., the primary's $v \sin(i) < 9$ km s $^{-1}$).

Bowler et al. (2023) have found using rotation period measurements from the primary that its orientation of the spin axis is most likely aligned with the plane of the orbit. In order to eliminate the degeneracy in inclination, we use the spin axis inclination of the star obtained by Bowler et al. (2023) to calculate the rotational velocity of each object.

We randomly sample from a Gaussian distribution with a mean of 66.5° and standard deviation of 10.8° for inclination measurements and from our $v \sin(i)$ and inclination chains for the companion (we keep the upper limit of 9 km s $^{-1}$ from

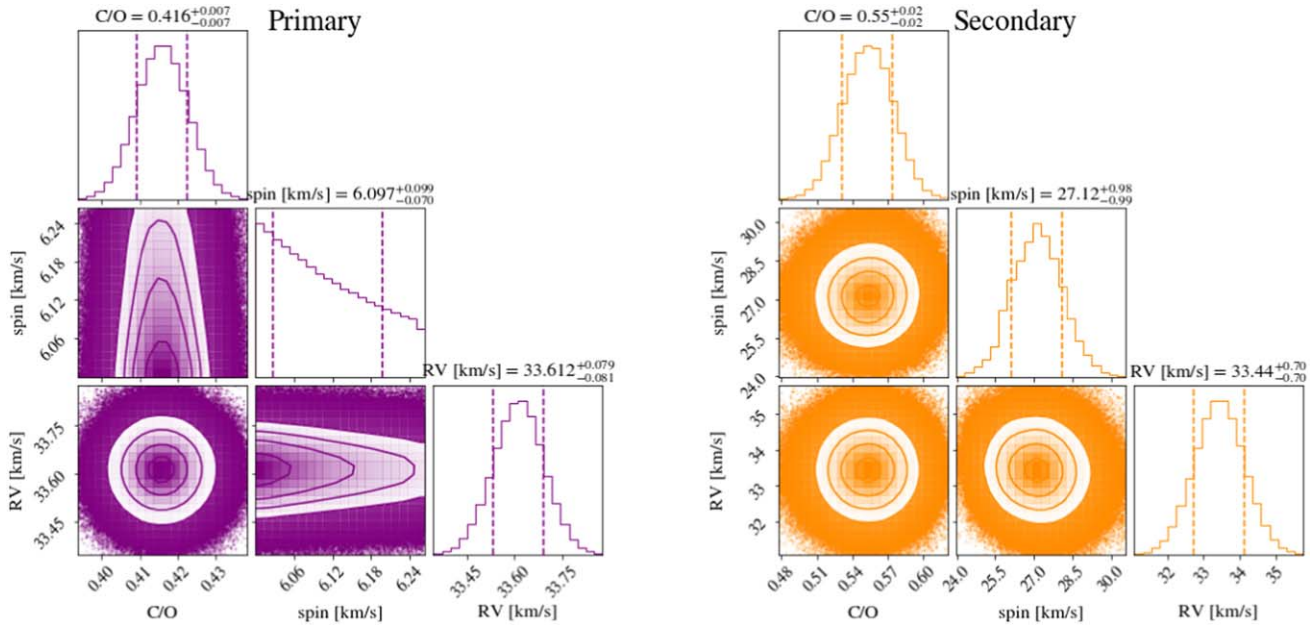


Figure 10. Final C/O ratio fit for the primary and secondary. We also include a fit for the spin and RV using this model grid and note that most values are broadly consistent with each other.

NIRSPEC as the host’s spin value) and obtain a distribution of rotational velocity of the companion and the host star. We find that the host star and the companion have very different rotational speeds, with $V_{\text{host}} \gtrsim 9 \text{ km s}^{-1}$ and $V_{\text{companion}} = 29.0^{+3.5}_{-3.5} \text{ km s}^{-1}$, yielding a ratio of $V_{\text{companion}}/V_{\text{host}} \gtrsim 3$. The companion is therefore spinning at least 3 times faster than the host star.

Breakup velocities can be calculated for an object with a given radius and mass using the equation:

$$v_{\text{break}} = \sqrt{\frac{GM}{R}} \quad (7)$$

where G is the gravitational constant, M is the object’s mass, and R is the object’s radius (e.g., Konopacky et al. 2012; Wang et al. 2021). We use this equation to estimate the breakup velocity of the primary and secondary. In order to perform this calculation, we estimate the radius of the targets using the same procedures to estimate the mass from evolutionary models by Baraffe et al. (2015; i.e., interpolating over the chains for temperature and $\log(g)$). We obtain radii of $0.39 \pm 0.10 R_{\odot}$ for the primary and $0.11 \pm 0.08 R_{\odot}$ for the secondary. Coupled with the masses obtained in Section 3.3, we obtain breakup velocities of $383 \pm 64 \text{ km s}^{-1}$ and $373 \pm 24 \text{ km s}^{-1}$, respectively. The two objects present similar breakup velocities, but the companion spins significantly faster than the host, at slightly above 8% of its breakup velocity, consistent with Bryan et al. (2020), who expect young companions to have spins at less than 10% of their breakup speed.

3.5. Summary of System Properties

We summarize the final derived system properties using Keck/KPIC data and Keck/NIRC2 data for the 1RXS J034231.8+121622 system. The properties are presented in Table 4.

Table 4
Final System Properties

Property	Host Star (Primary)	Companion (Secondary)
Temperature	$3460 \pm 50 \text{ K}$	$2510 \pm 50 \text{ K}$
$\log(g)$	4.94 ± 0.30	5.36 ± 0.30
[Fe/H]	0.16 ± 0.04	$0.13^{+0.12}_{-0.11}$
$v\sin(i)$	$< 9 \text{ km s}^{-1}$	$28.63^{+1.22}_{-1.13} \text{ km s}^{-1}$
Mass	0.30 ± 0.15	0.08 ± 0.01
Radius	$0.39 \pm 0.10 R_{\odot}$	$0.11 \pm 0.08 R_{\odot}$
Breakup Velocity	$383 \pm 64 \text{ km s}^{-1}$	$373 \pm 26 \text{ km s}^{-1}$
C/O	0.42 ± 0.10	0.55 ± 0.10

Note. The temperature, $\log(g)$, and C/O ratio present the inflated uncertainties. The mass, radius, and, consequently, breakup velocity are derived by interpolating temperature and $\log(g)$ measurements with evolutionary models from Baraffe et al. (2015).

4. Discussion

4.1. Temperature, $\log(g)$, and System Mass

Our resulting fits for KPIC data provide us with an insight on the host star and companion’s temperature, $\log(g)$, and [Fe/H] values. The final properties of these objects allow for a new system mass fit using evolutionary models. One particularly important change from previous results for the mass estimate for this system is the likely placement of this system as part of the Hyades found by Kuzuhara et al. (2022). The older age of 750 ± 100 Myr of the Hyades (Brandt & Huang 2015) places both the host and the companion at higher-mass estimates than previous measurements, which assumed an age of 60–300 Myr. The host star’s temperature and $\log(g)$ make it about 60% more massive than the previous estimate, while the companion is about 39% more massive than previous measurements. The mass ratio (companion/host), which was ≈ 0.17 , is now closer to 0.28.

For the companion, this new mass estimate places it near or above the hydrogen-burning limit, with the possibility of it being a low-mass star rather than a brown dwarf. Therefore, questions about the formation of this system’s secondary can be answered

using a variety of parameters, such as its orbital parameters (in particular the eccentricity) and atmospheric parameters.

4.2. Orbit Fit

The orbit fit of the companion presented significant changes once the new estimate in system mass, the NIRC2 astrometry, and the KPIC RV data points were incorporated. Without the addition of new data, the orbital fit had a large tail of high eccentricity and low inclination orbits approaching periastron passage. These posteriors are a result of a known bias when the orbital information is undersampled and the fit is prior dominated (e.g., O’Neil et al. 2019; Blunt et al. 2023; Do Ó et al. 2023). In particular, the eccentricity–inclination bias shown in Ferrer-Chávez et al. (2021) appears to apply to this system’s orbital posteriors, where it becomes difficult to distinguish between face-on, eccentric orbits and edge-on, circular orbits.

The change in system mass, however, also played a significant role on the final orbital posteriors. The possibility of major changes in orbital parameters with changing mass is briefly addressed by Bowler et al. (2020), who found that some companions in their orbit fits (including the one in this work) presented posteriors with a peak of eccentricities near 1.0 that could be caused by the wrong system mass estimate or underestimated astrometric uncertainties. Indeed, in this case no new astrometric or radial-velocity data were needed to significantly change the eccentricity posterior of the companion (and other posteriors as well, such as inclination and T_0). The reason for such a large difference in the companion’s orbit when changing the mass is Kepler’s third law: for a more massive system, the orbital velocities of the objects are also increased (i.e., they orbit faster around each other). Previously, the fast changing astrometry likely yielded an orbital velocity that, with a smaller system mass, could only be explained by an object that is at the fastest point in its orbit, i.e., the periastron passage. This required the orbit to be more eccentric and thus more “face-on” relative to our line of sight.

This result implies that the undersampling and uncertainty in “visual” orbital information, such as astrometry, is not the only contributor to the limitations in orbital characterization of directly imaged companions. Uncertainties in system age, distance, and, consequently, mass, which are all assumed to be known and held fixed or fit with a Gaussian prior in orbit fitting packages (O’Neil et al. 2019; Blunt et al. 2020; Brandt et al. 2021), also play a major role in the orbital determination of these objects and may be large.

The new KPIC RV data point is near zero, and therefore it is not sufficient to eliminate the degeneracy in Ω and ω , which would more accurately determine the orbital plane of the companion. However, it still provides valuable information for the orbit fit. Together with the new system mass, the new data place the orbit at a well-defined inclination of $\sim 83^\circ$, with the periastron passage occurring about 142 yr from the last observation. The period is ≈ 350 yr. In Appendix B, we present our uniform prior results, which are consistent with the observable prior results. Do Ó et al. (2023) found that the minimum orbital coverage required to obtain reliable orbital parameter posteriors is at about 15% of the orbital period. Therefore, despite the consistency in results regardless of prior choice, the orbit is still undersampled at about 4.3% of orbital period coverage. For that reason, there is a possibility that the orbital posteriors presented here will change with the addition of new data. It is also possible that the inclusion of radial-velocity data can decrease the coverage value needed to

leave the prior-dominated regime; however, that possibility is yet to be tested and should be explored in future work.

4.3. Metallicity

The metallicities for the primary and for the companion are 0.16 ± 0.04 and $0.13_{-0.11}^{+0.12}$, respectively. These metallicities indicate abundances slightly above the solar value of 0.012 (Asplund et al. 2006). These values also hint that this system likely formed in a region that is more metal rich. Indeed, the metal enrichment of the Hyades ([Fe/H] varies between 0.11 and 0.21; e.g., Perryman et al. 1998; Maderak et al. 2013; Brandner et al. 2023) further contributes to the likely association of this system with the cluster stipulated by Bowler et al. (2015b) and Kuzuhara et al. (2022). We repeat the procedure performed by Kuzuhara et al. (2022) using the BANYAN- Σ algorithm (Gagné et al. 2018) with the updated radial velocity for the system from KPIC and obtain a Hyades membership probability of 99.8%. The newfound Hyades membership also imposes better constraints on age and distance to the system, which improve both mass and orbit estimates for the objects.

4.4. C/O Ratio

The C/O ratios obtained for the host star and the secondary are 0.42 and 0.55, respectively. Utilizing uncertainties that account for potential systematics in the models themselves of ± 0.1 , these two values are broadly consistent with each other (about 1σ away), and the primary’s value is broadly consistent with the Sun’s C/O ratio of 0.59 found by Asplund et al. (2021). Despite the fact that the new larger mass of the companion means that this source could not have formed via core accretion (see Section 4.6), there are two reasons why this measurement is still helpful. First, it provides a means for verifying the C/O ratios of other sources (e.g., Phillips et al. 2024). If the measured values had been significantly different from each other or from the solar value, it may have called into question measurements for planets in which C/O is not near 0.59. Thus, systems such as this one verify the expectation of chemical homogeneity between companion and star and provide important cross-checks for objects with similar spectral features that may have formed via core/pebble accretion. Second, it places this object in the broader context of other systems in which C/O is being measured, allowing for the investigation of potential values of C/O across the full mass spectrum of measured companions. Additional data points at higher masses will help to more strongly identify any breaks in C/O as a function of properties such as mass, separation, and/or age (e.g., Hoch et al. 2023).

4.5. Rotational Velocity

The objects’ rotational velocities were assessed assuming alignment of the rotational axis with the orbital plane. We find that the objects have very different spin velocities, of at most 9 km s^{-1} for the host star and $\sim 29 \text{ km s}^{-1}$ for the companion. The companion spins at least ~ 3 times faster than the host star, which is consistent with the theoretical predictions of magnetic braking timescales for lower-mass objects (e.g., West et al. 2008). The longer timescales for magnetic braking laws cause objects of lower mass to often be rapid rotators (e.g., Konopacky et al. 2012), and can explain the discrepancy in rotational velocities of the host and the companion. For instance, Reiners & Basri (2008) found that mid-M dwarfs are slow rotators while late-M dwarfs are fast rotators, with the rotation speed being strongly correlated

with an object's magnetic field. West et al. (2008) quantified this process by generating an age–activity relationship for M dwarfs. The temperature of the primary places it in an early-M spectral type. The companion's temperature places it in a late-M spectral type (Pecaut & Mamajek 2013). With these spectral types, West et al. (2008) predict an activity lifetime of about 2 ± 0.5 Gyr for the primary and over 8 Gyr for the secondary. After estimating the breakup velocities of both objects, the companion is only spinning at $\sim 8\%$ of its breakup velocity, which is less than a few objects found by Konopacky et al. (2012), for instance, which were spinning at $\sim 30\%$ of their breakup speed.

4.6. Formation Pathways

The RXS J034231.8+121622 system is composed of an M dwarf host star with a massive companion at or about the hydrogen-burning limit. The C/O ratios of both components are similar to each other, with no C/O enhancement in the companion. This is expected since theoretical scenarios predict difficulty in forming objects above $\sim 30 M_{\text{Jup}}$ via core or pebble accretion, particularly around low-mass stars (e.g., Mordasini et al. 2012; Schlecker et al. 2022). However, sources such as 1RXS0342+1216 b may be candidates for formation via gravitational instability in a disk. Using the predictions of Kratter et al. (2010) for the potential mass of an object that can be formed via disk instability, we find that companions as large as $153 M_{\text{Jup}}$ are feasible at the best-fit semimajor axis of ~ 36 au. Thus, exploring whether higher-mass companions formed via gravitational instability in a disk versus a binary star formation scenario is an interesting area of investigation, especially in the context of understanding the full spectrum of outcomes for the companion formation process.

However, distinguishing between disk instability and binary star formation mechanisms (e.g., disk fragmentation) is a challenging task. For example, the eccentricity of the companion is moderate, at about 0.4. Despite the potential usefulness of the eccentricity parameter as a formation tracer at a population level, it is difficult to determine formation pathways for an individual system by assessing the eccentricity alone, because gravitational instability has been found to produce clumps of eccentricities as high as 0.35 in simulations (Mayer et al. 2004), and binary star formation studies have found that close binary stars of < 100 au separation have uniform population eccentricity distributions (Hwang et al. 2022).

5. Conclusion

This work characterizes the 1RXS J034231.8+121622 system using high-resolution spectroscopy from the Keck Planet Imager and Characterizer (KPIC) and a new astrometry data point from Keck/NIRC2. The main findings of this study are:

1. We find the temperature, $\log(g)$, [Fe/H], spin, RV, and C/O ratio for both the host star and the companion. The relative RVs, spins, and C/O ratios are reported for the first time for this system (see Table 4).
2. We use the temperature and $\log(g)$ posteriors to re-derive the masses of these objects using an updated age for the system, which is now older than previously derived due to its likely association with the Hyades (750 ± 100 Myr). The [Fe/H] measurement is well in agreement with the Hyades value. The masses of both objects increased, by 60% for the host star and by 39% for the companion.
3. We find that the system mass, which is generally taken as a fixed parameter or fit for using a Gaussian prior in orbit

fits, changes our orbital parameter posteriors substantially even without the addition of new astrometry or radial velocities. The increase in system mass causes the periastron passage of the companion to be further away in time from observations.

4. The orbital parameter posteriors for the companion hint at a moderate eccentricity of ~ 0.4 –0.5, a result that appears to be independent of priors. The tails of low eccentricities (< 0.2) and high eccentricities (> 0.9) are now disfavored by the addition of new data. However, the eccentricity distribution is still uncertain and will likely require further observations to better constrain it.
5. The C/O ratios for the host and the companion are 0.42 ± 0.10 and 0.55 ± 0.10 . Both values are broadly consistent with solar values.
6. Previous works have found that the companion and the host spin axis are likely aligned with the orbital axis. If this is the case, the companion is spinning at least 3 times faster than the host, as is expected for lower-mass objects. The companion spins at about 8% of its breakup velocity.
7. From the eccentricity, mass ratio, and C/O ratio of the objects, the formation of this system did not occur from a core accretion scenario. Whether it occurred via gravitational instabilities in a protoplanetary disk or disk fragmentation in a protostellar disk remains unclear.

This work shows that high-resolution spectroscopy is a powerful tool for characterizing directly imaged systems. The high-resolution spectra allowed for precise radial-velocity measurements of substellar companions and for atmospheric parameter estimation such as temperature, $\log(g)$, [Fe/H], spin, and C/O ratio. Together, the detailed characterization of these systems provides clues on the formation processes of these companions, both individually and at a population level.

Acknowledgments

We thankfully acknowledge Brendan Bowler for sharing OSIRIS data on 1RXS J034231.8+121622. We also thank the anonymous referee for providing comments that helped improve this manuscript.

Some of the data presented herein were obtained at the W. M. Keck Observatory, which is operated as a scientific partnership among the California Institute of Technology, the University of California, and the National Aeronautics and Space Administration. The W. M. Keck Observatory was made possible by the financial support of the W. M. Keck Foundation. The authors wish to acknowledge the significant cultural role that the summit of Maunakea has always had within the indigenous Hawaiian community. The authors are extremely fortunate to conduct observations from this mountain. Portions of this work were conducted at the University of California, San Diego, which was built on the unceded territory of the Kumeyaay Nation, whose people continue to maintain their political sovereignty and cultural traditions as vital members of the San Diego community.

C.D.O. is supported by the National Science Foundation Graduate Research Fellowship under grant No. DGE-2038238. Further support for this work at UCLA was provided by the W. M. Keck Foundation, and NSF Grant No. AST-1909554. J.X. acknowledges support from the NASA Future Investigators in NASA Earth and Space Science and Technology (FINESST) award #80NSSC23K1434. Any opinions, findings, and conclusions or recommendations expressed in this material are those of

the author(s) and do not necessarily reflect the views of the National Science Foundation.

Funding for KPIC has been provided by the California Institute of Technology, the Jet Propulsion Laboratory, the Heising-Simons Foundation (grants #2015-129, #2017-318, #2019-1312, and #2023-4598), the Simons Foundation (through the Caltech Center for Comparative Planetary Evolution), and the NSF under grant No. AST-1611623.

Part of this work was carried out at the Jet Propulsion Laboratory, California Institute of Technology, under contract with NASA (80NM00018D0004).

Appendix A Full Corner Plots

In this section we present the full corner plots for the companion's orbit fit with different amounts of data. The orbit fit with the old system mass and no additional data can be found in Figure 11. Figure 12 shows the orbit fit with no additional data but with the new system mass. The orbit fit with a new astrometry epoch from Keck/NIRC2 can be found in Figure 13. Figure 14 shows the orbit fit with an RV point from Keck/KPIC.

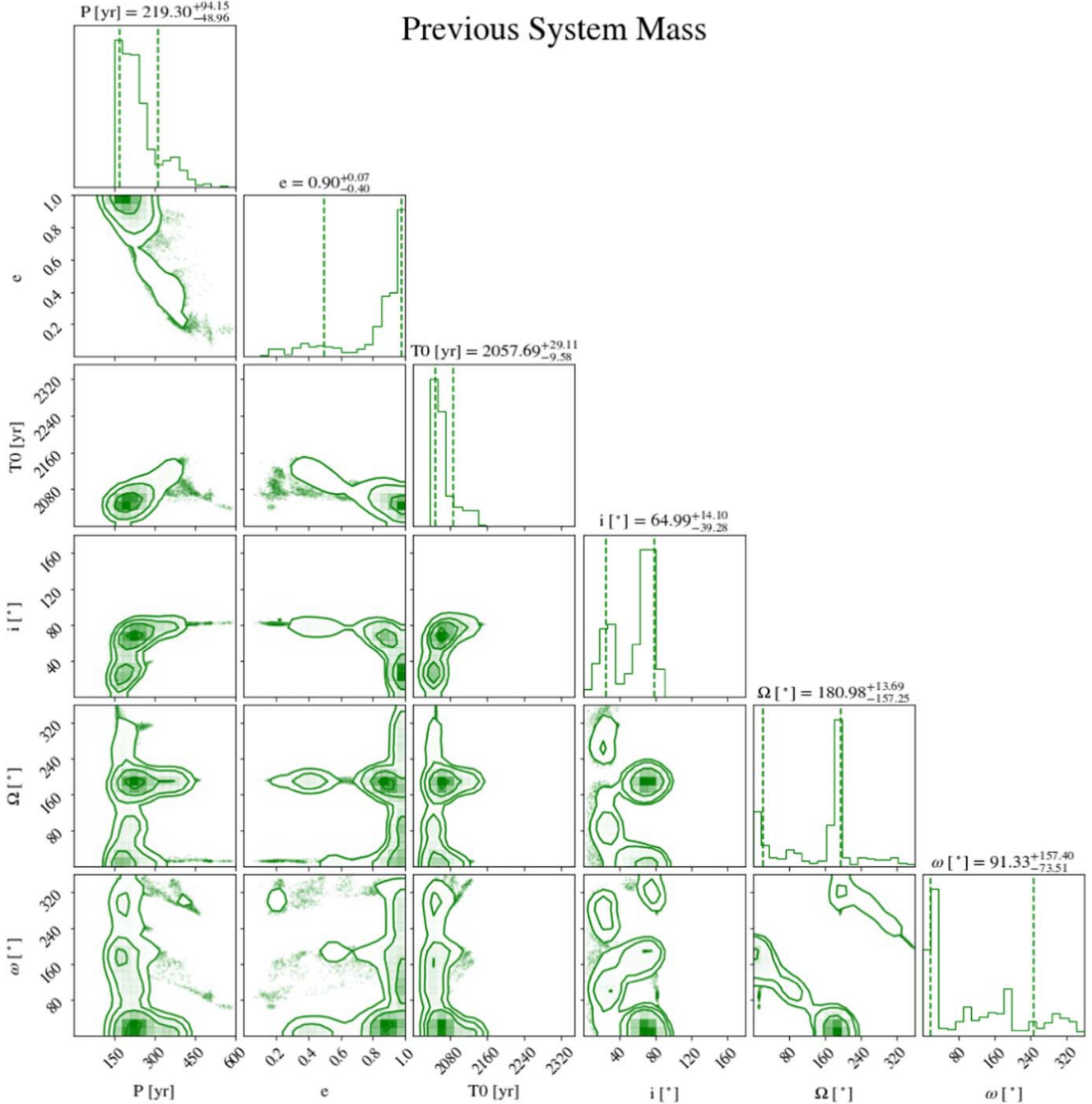


Figure 11. Corner plots for 1RXS0342+1216 b's orbital parameters with the previous system mass of $0.23 M_\odot$. No new astrometry or radial-velocity data were included in this orbit fit.

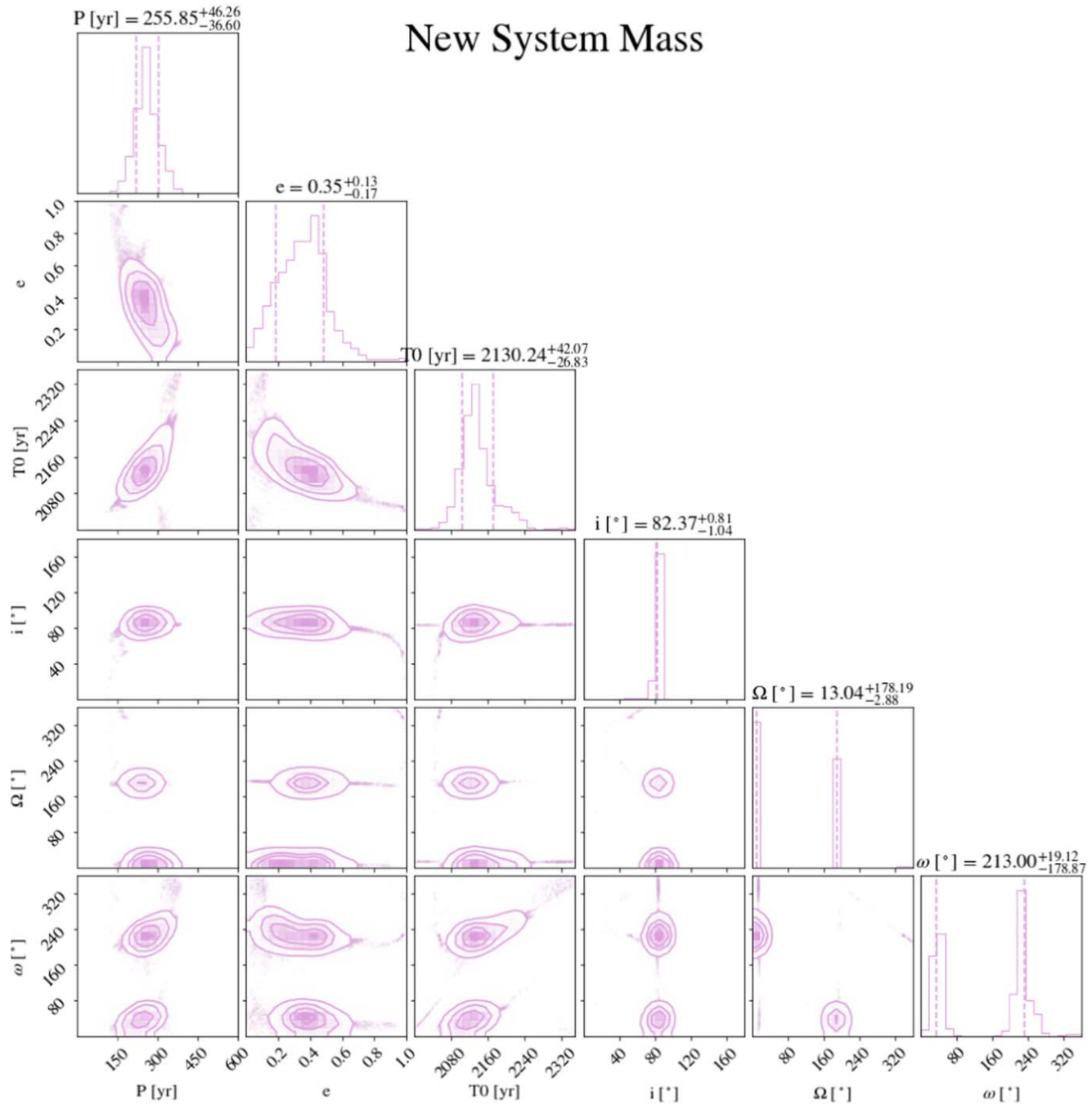


Figure 12. Corner plots for 1RXS0342+1216 b's orbital parameters with the new system mass of $0.38 M_{\odot}$. No new astrometry or radial-velocity data were included in this orbit fit.

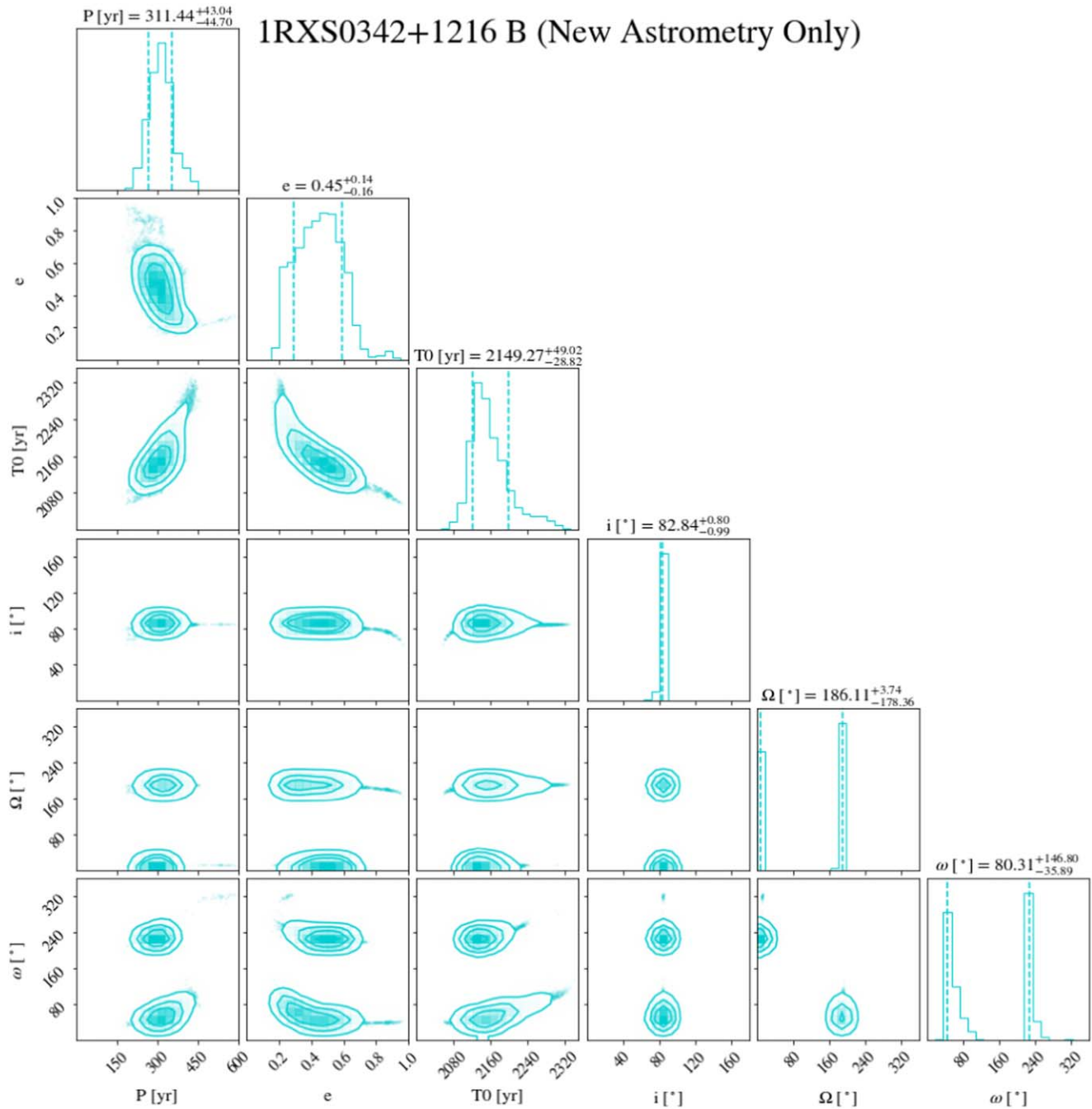


Figure 13. New orbit fit of 1RXS0342+1216 with the new 2023A astrometry epoch.

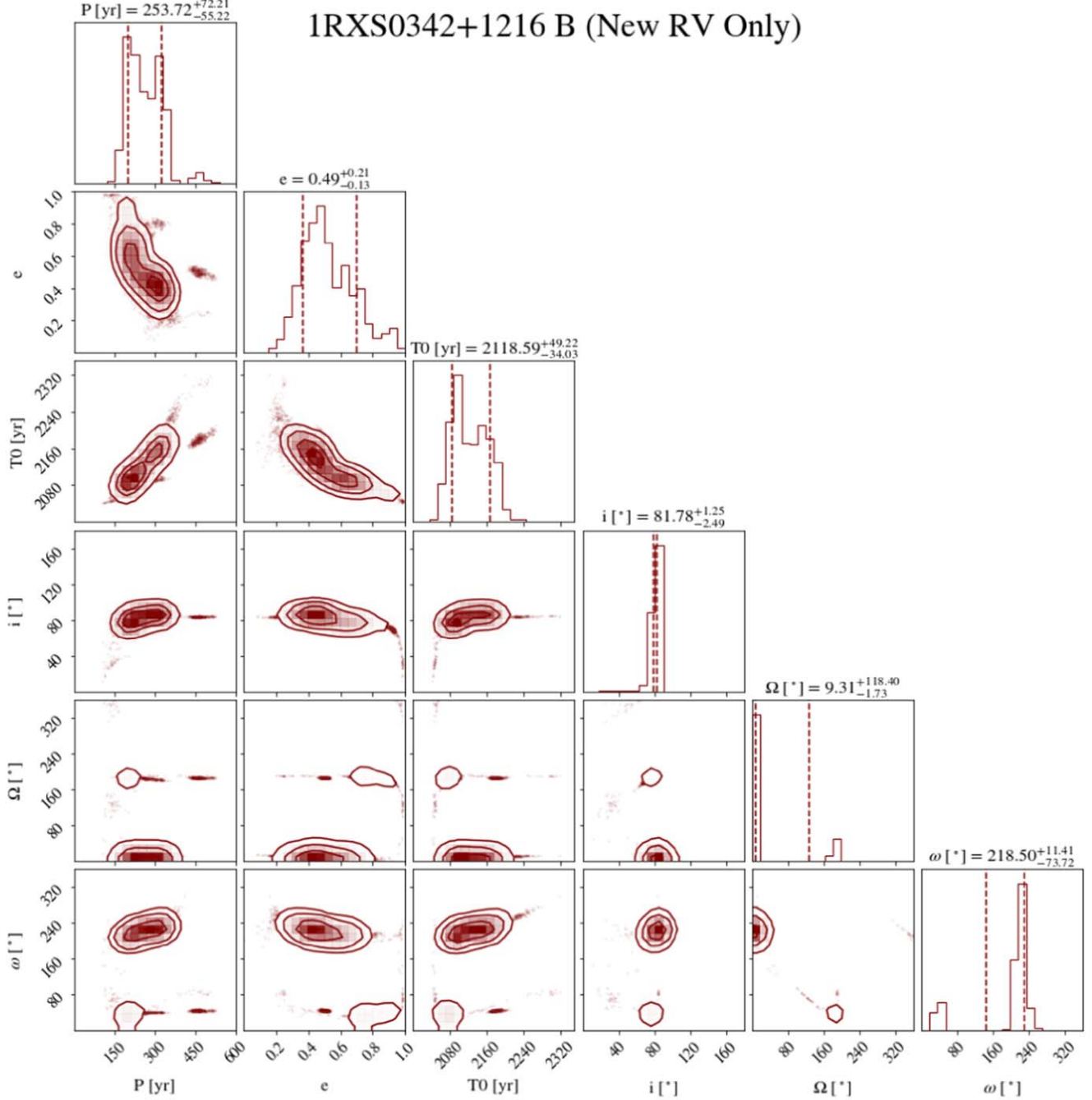


Figure 14. New orbit fit of 1RXS0342+1216 with the 2020 RV data point. Although RV data have the ability to break the degeneracy in the orientation of the orbital plane, the relative RV between the primary and the secondary in the 2020 epoch was close to 0 km s^{-1} , meaning that we are not able to resolve that degeneracy with our data.

Appendix B Uniform Priors Fit

In this section, we present our results for the orbit fit of the companion with the traditionally used uniform parameter priors. We split our results into two main subsections: testing system mass changes and the final orbit fit with the NIRC2 astrometry point from 2023A and KPIC RV from 2020 incorporated in the fit. We run the uniform priors with Efit5 as was done for the observable-based prior run as well as with orbitize! (Blunt et al. 2020). The interest in using both methods is because Efit5 uses a nested sampling algorithm, MULTINEST, while orbitize! uses a Markov Chain Monte Carlo approach. orbitize! also intakes a Gaussian prior for the system mass, while Efit5 holds the mass

fixed at a single value. We aim to verify that both approaches show similar results in the orbital posteriors.

B.1. Change in System Mass

We run our fits with uniform priors for the old total system mass of $0.23 M_{\odot}$. Our results for both the orbitize! and the Efit5 runs are shown in Figure 15. We note that in both cases there is a tail of high eccentricities coupled with lower inclinations. In both cases lower eccentricity solutions are also found, which is not the case for the observable prior fit. When the new system mass is incorporated, both tails of high eccentricity are less significant in the orbital fit, with the Efit5 fit's eccentricity tail completely disappearing, similar to the observable prior case.

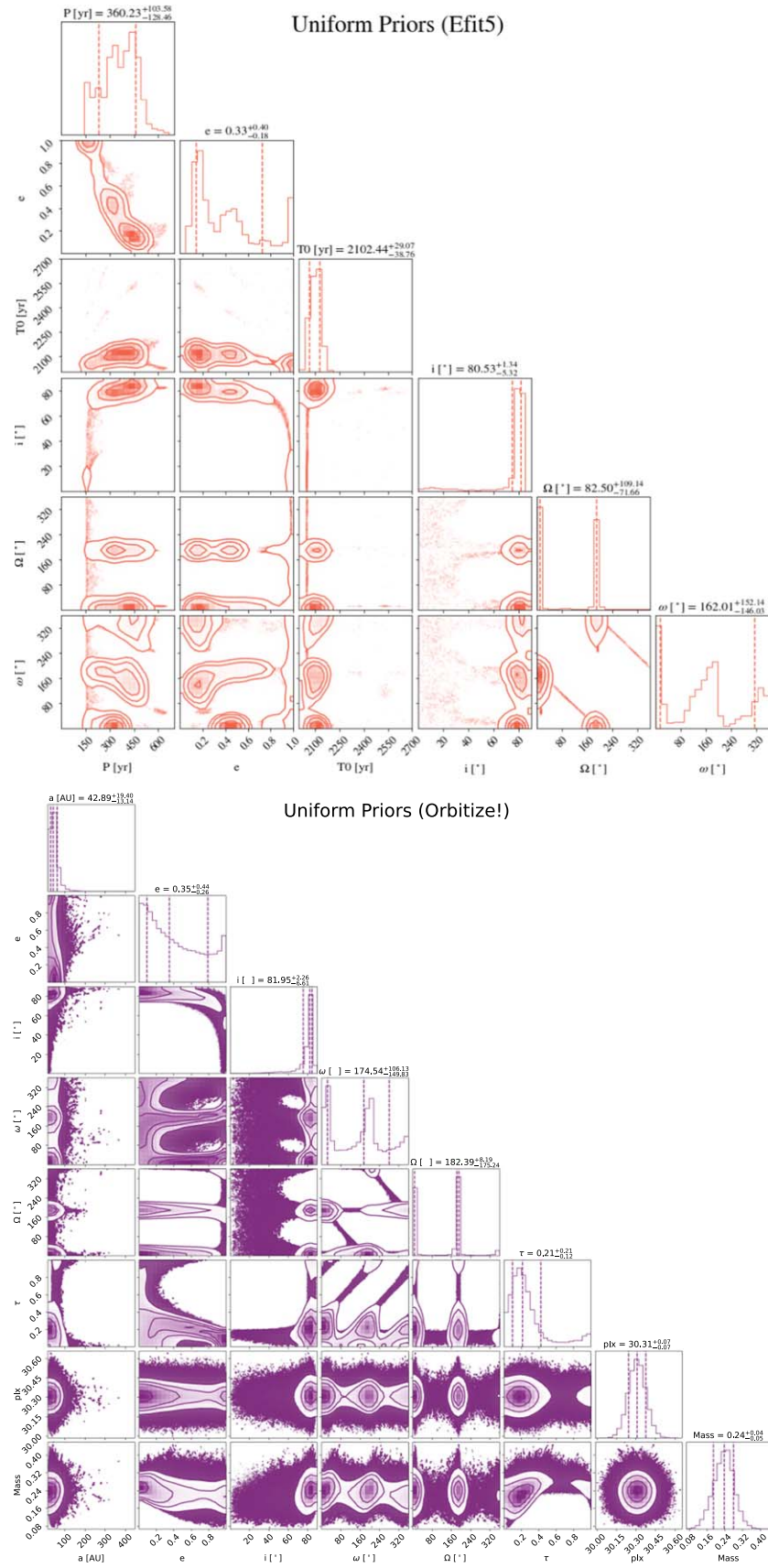


Figure 15. Uniform prior fit with Efit5 and orbitize! for the previous system mass of $0.23 M_\odot$.

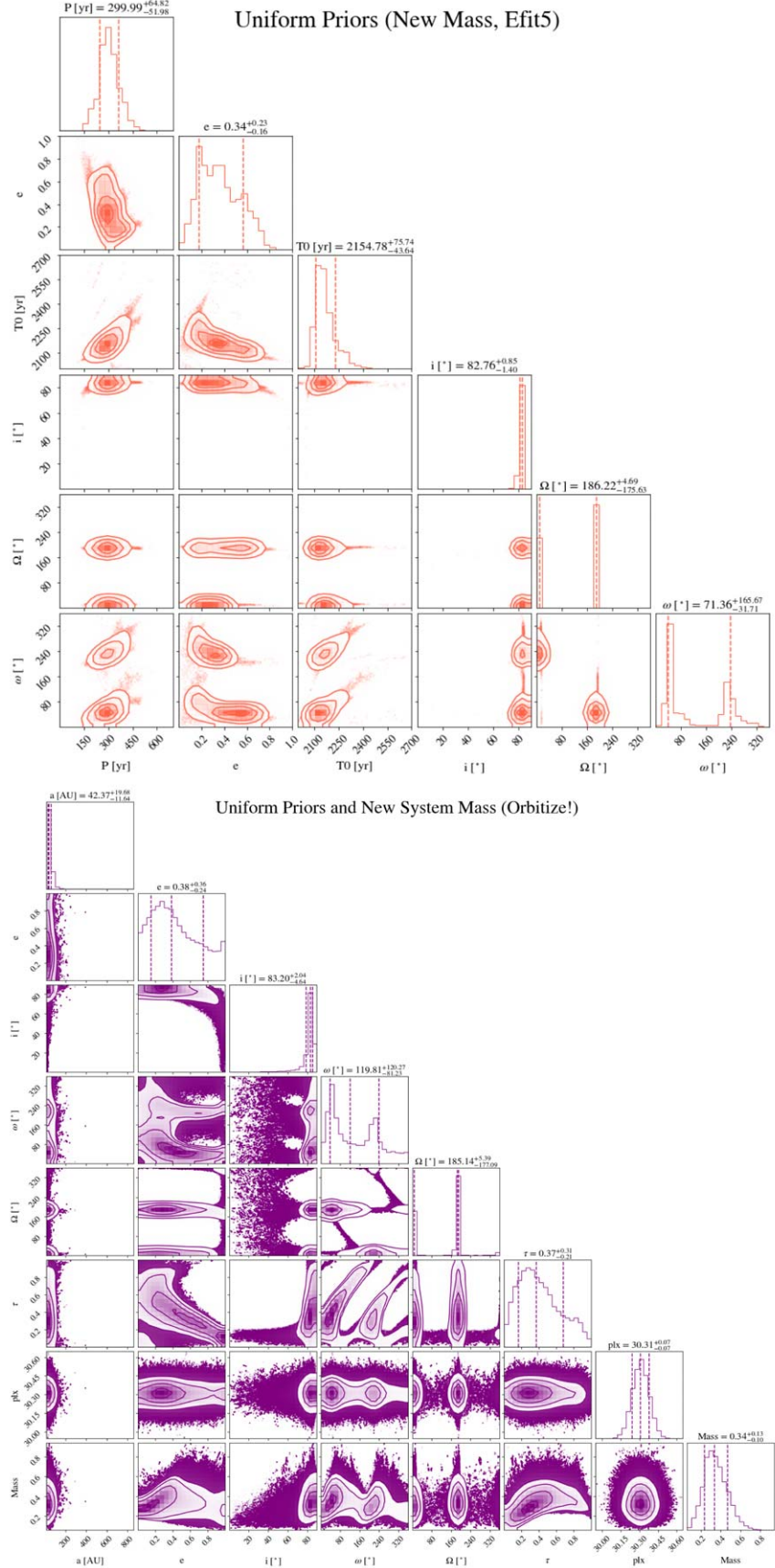


Figure 16. Uniform prior fit with Efit5 and Orbitize! for the new system mass of $0.38 M_{\odot}$.

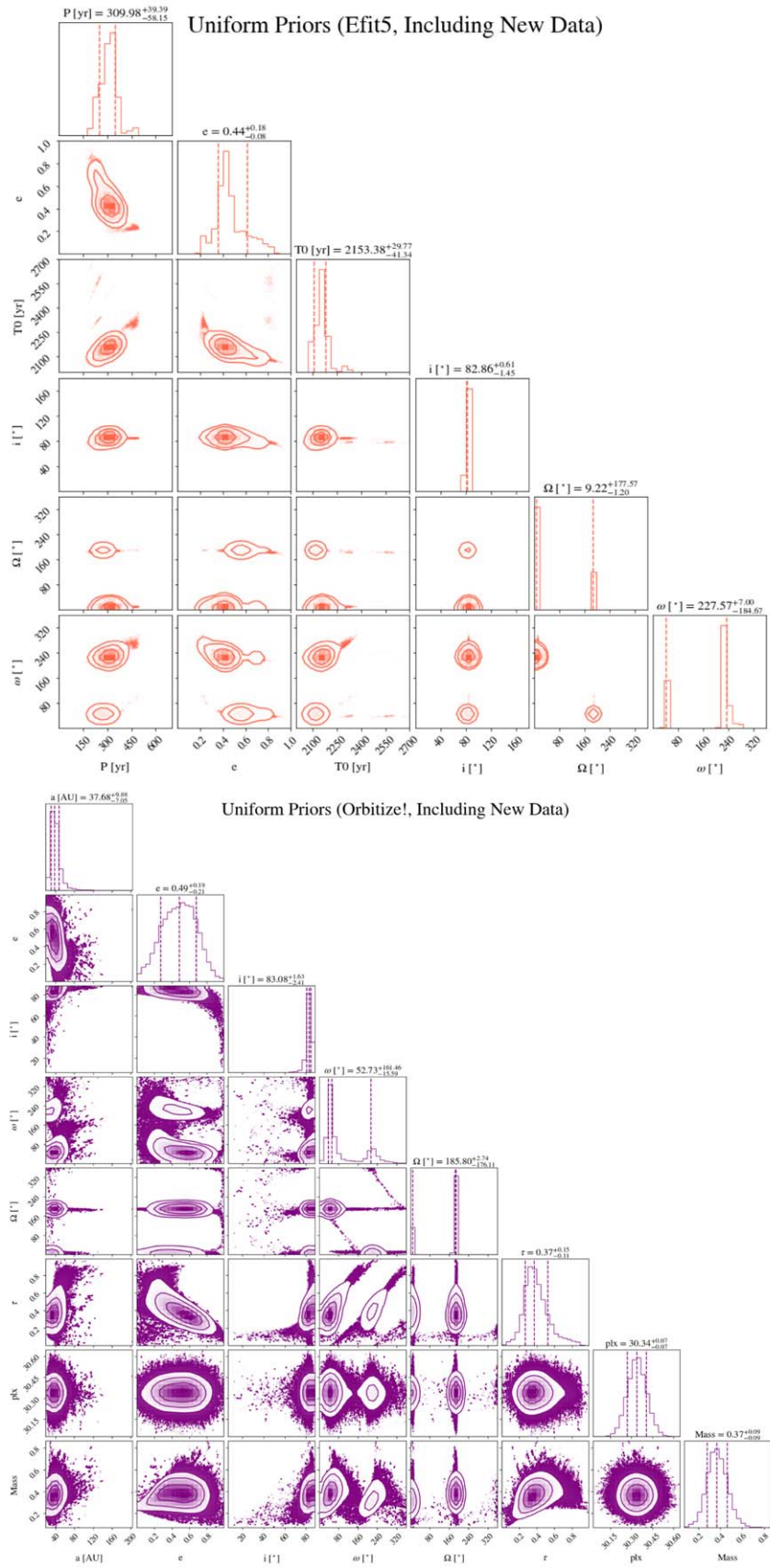


Figure 17. Uniform prior fit with Efit5 and orbitize! for the new system mass of $0.38 M_{\odot}$, new 2023A astrometry data point from NIRC2, and 2020 RV data point from KPIC.

Figure 16 shows the orbit fit with the new system mass and no additional data using uniform priors.

B.2. Addition of New Data

With the addition of new data, the uniform prior fits show similar results in their posteriors. The corner plot results are shown in Figure 17. In both cases, moderate eccentricities are favored by the data, as is the case for observable priors. The inclinations all agree with a nearly edge-on configuration of $i \sim 82^\circ$.

Appendix C Mass as a Free Parameter

We also run the orbit fit with observable priors making the mass a free parameter with a uniform prior (Figure 18). We obtain similar posteriors as with a fixed mass for the orbital parameters. The eccentricity is slightly lower than with a fixed mass (0.38 versus 0.41), and the periastron passage is about 15 yr sooner. The mass obtained with models of $0.38 M_\odot$ is well within the uncertainties given by the fit of $0.30^{+0.12}_{-0.06} M_\odot$, which disfavors the previous system mass estimate of $0.23 M_\odot$.

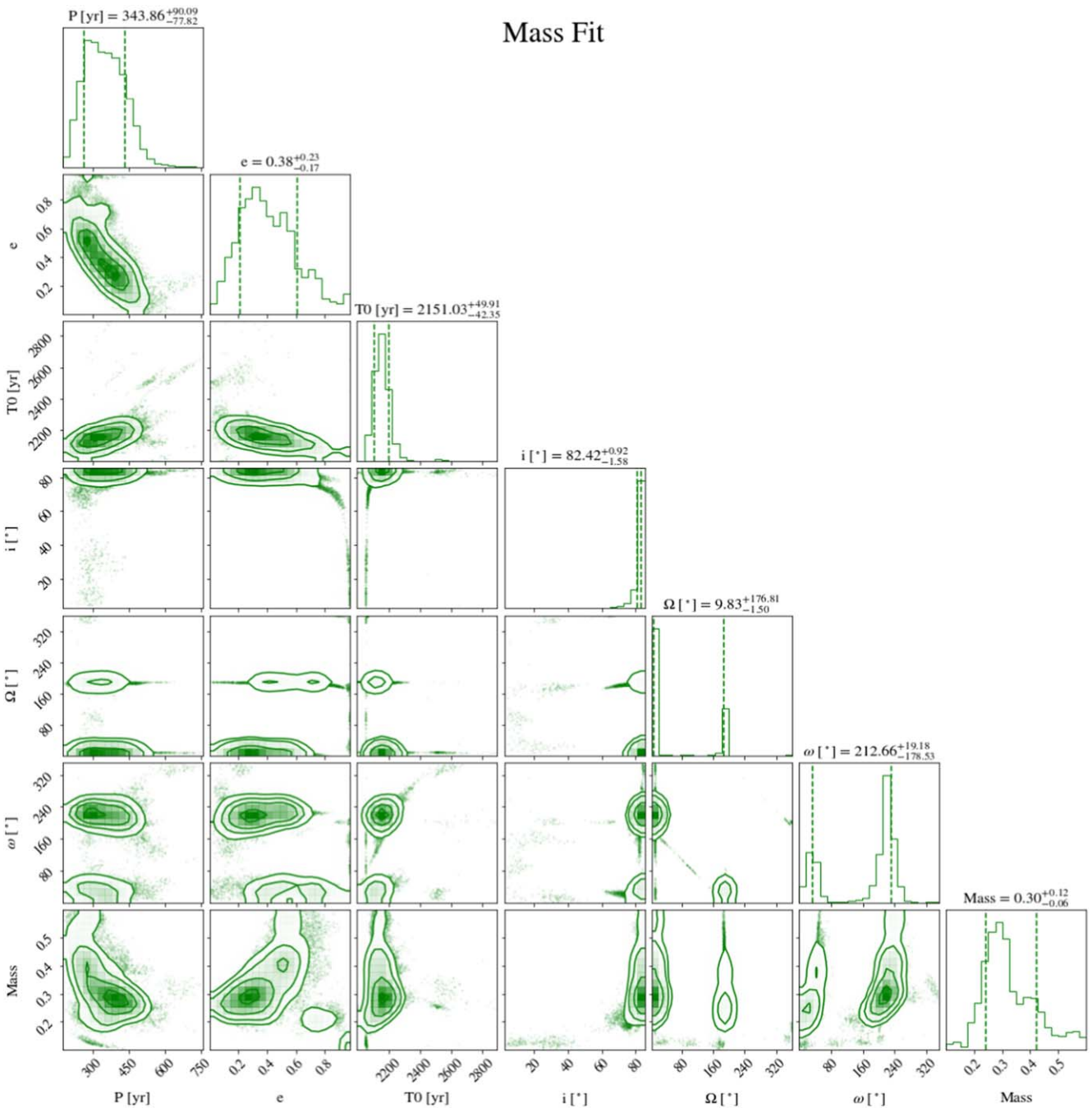


Figure 18. Posteriors for Efit5 with the new data and uniform prior mass fit. Orbital parameters are fit with observable priors.

ORCID iDs

Clarissa R. Do Ó <https://orcid.org/0000-0001-5173-2947>
 Ben Sappéy <https://orcid.org/0000-0003-1399-3593>
 Quinn M. Konopacky <https://orcid.org/0000-0002-9936-6285>
 Jean-Baptiste Ruffio <https://orcid.org/0000-0003-2233-4821>
 Kelly K. O'Neil <https://orcid.org/0000-0003-2400-7322>
 Tuan Do <https://orcid.org/0000-0001-9554-6062>
 Gregory Martinez <https://orcid.org/0000-0002-7476-2521>
 Travis S. Barman <https://orcid.org/0000-0002-7129-3002>
 Jayke S. Nguyen <https://orcid.org/0000-0002-9242-9052>
 Jerry W. Xuan <https://orcid.org/0000-0002-6618-1137>
 Christopher A. Theissen <https://orcid.org/0000-0002-9807-5435>
 Sarah Blunt <https://orcid.org/0000-0002-3199-2888>
 William Thompson <https://orcid.org/0000-0001-5684-4593>
 Chih-Chun Hsu <https://orcid.org/0000-0002-5370-7494>
 Geoffrey A. Blake <https://orcid.org/0000-0003-0787-1610>
 Benjamin Calvin <https://orcid.org/0000-0003-4737-5486>
 Jacques-Robert Delorme <https://orcid.org/0000-0001-8953-1008>
 Daniel Echeverri <https://orcid.org/0000-0002-1583-2040>
 Luke Finnerty <https://orcid.org/0000-0002-1392-0768>
 Michael P. Fitzgerald <https://orcid.org/0000-0002-0176-8973>
 Julie Inglis <https://orcid.org/0000-0001-9164-7966>
 Nemanja Jovanovic <https://orcid.org/0000-0001-5213-6207>
 Ronald A. López <https://orcid.org/0000-0002-2019-4995>
 Dimitri Mawet <https://orcid.org/0000-0002-8895-4735>
 Evan Morris <https://orcid.org/0000-0003-3165-0922>
 Andrew Skemer <https://orcid.org/0000-0001-6098-3924>
 J. Kent Wallace <https://orcid.org/0000-0001-5299-6899>
 Jason J. Wang <https://orcid.org/0000-0003-0774-6502>
 Ji Wang <https://orcid.org/0000-0002-4361-8885>
 Joshua Liberman <https://orcid.org/0000-0002-4934-3042>

References

Agrawal, S. 2022, Senior thesis (Major), California Institute of Technology, doi:[10.7907/17sv-vf40](https://doi.org/10.7907/17sv-vf40)

Anderson, K. R., Lai, D., & Storch, N. I. 2017, *MNRAS*, **467**, 3066

Asplund, M., Amarsi, A. M., & Grevesse, N. 2021, *A&A*, **653**, A141

Asplund, M., Grevesse, N., & Sauval, A. J. 2006, *CoAst*, **147**, 76

Bailer-Jones, C. A. L., Rybizki, J., Fouesneau, M., Demleitner, M., & Andrae, R. 2021, *AJ*, **161**, 147

Baraffe, I., Chabrier, G., Allard, F., & Hauschildt, P. H. 1998, *A&A*, **337**, 403

Baraffe, I., Chabrier, G., Barman, T. S., Allard, F., & Hauschildt, P. H. 2003, *A&A*, **402**, 701

Baraffe, I., Homeier, D., Allard, F., & Chabrier, G. 2015, *A&A*, **577**, A42

Blake, C. H., Charbonneau, D., & White, R. J. 2010, *ApJ*, **723**, 684

Blunt, S., Balmer, W. O., Wang, J. J., et al. 2023, *AJ*, **166**, 257

Blunt, S., Wang, J. J., Angelo, I., et al. 2020, *AJ*, **159**, 89

Boss, A. P. 2010, in IAU Symp. 265, Chemical Abundances in the Universe: Connecting First Stars to Planets, ed. K. Cunha, M. Spite, & B. Barbuy, Vol. 265 (Cambridge: Cambridge Univ. Press), 391

Bowler, B. P., Blunt, S. C., & Nielsen, E. L. 2020, *AJ*, **159**, 63

Bowler, B. P., Liu, M. C., Shkolnik, E. L., & Tamura, M. 2015a, *ApJS*, **216**, 7

Bowler, B. P., Shkolnik, E. L., Liu, M. C., et al. 2015b, *ApJ*, **806**, 62

Bowler, B. P., Tran, Q. H., Zhang, Z., et al. 2023, *AJ*, **165**, 164

Brandner, W., Calissendorff, P., & Kopytova, T. 2023, *AJ*, **165**, 108

Brandt, T. D., Dupuy, T. J., Li, Y., et al. 2021, *AJ*, **162**, 186

Brandt, T. D., & Huang, C. X. 2015, *ApJ*, **807**, 24

Browning, M. K. 2008, *ApJ*, **676**, 1262

Bryan, M. L., Chiang, E., Morley, C. V., Mace, G. N., & Bowler, B. P. 2021, *AJ*, **162**, 217

Bryan, M. L., Ginzburg, S., Chiang, E., et al. 2020, *ApJ*, **905**, 37

Burrows, A., Hubbard, W. B., Lunine, J. I., & Liebert, J. 2001, *RvMP*, **73**, 719

Chatterjee, S., Ford, E. B., Matsumura, S., & Rasio, F. A. 2008, *ApJ*, **686**, 580

Del Burgo, C., Martín, E. L., Zapatero Osorio, M. R., & Hauschildt, P. H. 2009, *A&A*, **501**, 1059

Delorme, J.-R., Jovanovic, N., Echeverri, D., et al. 2021, *JATIS*, **7**, 035006

Diolaiti, E., Bendinelli, O., Bonaccini, D., et al. 2000, *Proc. SPIE*, **4007**, 879

Do Ó, C. R., O'Neil, K. K., Konopacky, Q. M., et al. 2023, *AJ*, **166**, 48

Echeverri, D., Jovanovic, N., Delorme, J.-R., et al. 2022, *Proc. SPIE*, **12184**, 121841W

Epstein-Martin, M., Becker, J., & Batygin, K. 2022, *ApJ*, **931**, 42

Feroz, F., & Hobson, M. P. 2008, *MNRAS*, **384**, 449

Feroz, F., Hobson, M. P., & Bridges, M. 2009, *MNRAS*, **398**, 1601

Ferrer-Chávez, R., Wang, J. J., & Blunt, S. 2021, *AJ*, **161**, 241

Foreman-Mackey, D., Hogg, D. W., Lang, D., & Goodman, J. 2013, *PASP*, **125**, 306

Fruchter, A. S., & Hook, R. N. 2002, *PASP*, **114**, 144

Gagné, J., Mamajek, E. E., Malo, L., et al. 2018, *ApJ*, **856**, 23

Gaia Collaboration, Brown, A. G. A., Vallenari, A., et al. 2018, *A&A*, **616**, A1

Ghez, A. M., Becklin, E., Duchêne, G., et al. 2003, *ANS*, **324**, 527

Hartkopf, W. I., McAlister, H. A., & Franz, O. G. 1989, *AJ*, **98**, 1014

Helled, R., & Schubert, G. 2009, *ApJ*, **697**, 1256

Herbst, W., Eislöffel, J., Mundt, R., & Scholz, A. 2007, in *Protostars and Planets V*, ed. B. Reipurth, D. Jewitt, & K. Keil (Tucson, AZ: Univ. Arizona Press), 297

Hilditch, R. W. 2001, *An Introduction to Close Binary Stars* (Cambridge: Cambridge Univ. Press)

Hoch, K. K. W., Konopacky, Q. M., Barman, T. S., et al. 2022, *AJ*, **164**, 155

Hoch, K. K. W., Konopacky, Q. M., Theissen, C. A., et al. 2023, *AJ*, **166**, 85

Hsu, C.-C., Burgasser, A. J., Theissen, C. A., et al. 2024, arXiv:[2403.13760](https://arxiv.org/abs/2403.13760)

Hsu, C.-C., Theissen, C., Burgasser, A., & Birkby, J. 2021a, SMART: The Spectral Modeling Analysis and RV Tool, v1.0.0, Zenodo, doi:[10.5281/zenodo.4765258](https://doi.org/10.5281/zenodo.4765258)

Hsu, C.-C., Burgasser, A. J., Theissen, C. A., et al. 2021b, *ApJS*, **257**, 45

Husser, T. O., Wende-von Berg, S., Dreizler, S., et al. 2013, *A&A*, **553**, A6

Hwang, H.-C., Ting, Y.-S., & Zakamska, N. L. 2022, *MNRAS*, **512**, 3383

Janson, M., Bergfors, C., Brandner, W., et al. 2014, *ApJS*, **214**, 17

Janson, M., Hormuth, F., Bergfors, C., et al. 2012, *ApJ*, **754**, 44

Kipping, D. M. 2013, *MNRAS*, **434**, L51

Konopacky, Q. M., Barman, T. S., Macintosh, B. A., & Marois, C. 2013, *Sci*, **339**, 1398

Konopacky, Q. M., Ghez, A. M., Fabrycky, D. C., et al. 2012, *ApJ*, **750**, 79

Konopacky, Q. M., Marois, C., Macintosh, B. A., et al. 2016, *AJ*, **152**, 28

Kratter, K. M., Murray-Clay, R. A., & Youdin, A. N. 2010, *ApJ*, **710**, 1375

Kuzuhara, M., Currie, T., Takarada, T., et al. 2022, *ApJL*, **934**, L18

Landman, R., Stolker, T., Snellen, I. A. G., et al. 2024, *A&A*, **682**, A48

López, R. A., Hoffman, E. B., Doppmann, G., et al. 2020, *Proc. SPIE*, **11447**, 114476B

Maderak, R. M., Deliyannis, C. P., King, J. R., & Cummings, J. D. 2013, *AJ*, **146**, 143

Martin, E. C., Fitzgerald, M. P., McLean, I. S., et al. 2018, *Proc. SPIE*, **10702**, 107020A

Martinez, G. D., Kosmo, K., Hees, A., Ahn, J., & Ghez, A. 2017, in *IAU Symp. 322, The Multi-Messenger Astrophysics of the Galactic Centre*, ed. R. M. Crocker, S. N. Longmore, & G. V. Bicknell, 322 (Cambridge: Cambridge Univ. Press), 239

Mayer, L., Quinn, T., Wadsley, J., & Stadel, J. 2004, *ApJ*, **609**, 1045

McLean, I. S., Graham, J. R., Becklin, E. E., et al. 2000, *Proc. SPIE*, **4008**, 1048

Meyer, L., Ghez, A. M., Schödel, R., et al. 2012, *Sci*, **338**, 84

Mohanty, S., & Basri, G. 2003, *ApJ*, **583**, 451

Mordasini, C., Alibert, Y., Benz, W., Klahr, H., & Henning, T. 2012, *A&A*, **541**, A97

Morley, C. V., Mukherjee, S., Marley, M. S., et al. 2024, arXiv:[2402.00758](https://arxiv.org/abs/2402.00758)

Mukherjee, S., Fortney, J. J., Morley, C. V., et al. 2024, arXiv:[2402.00756](https://arxiv.org/abs/2402.00756)

Nagpal, V., Blunt, S., Bowler, B. P., et al. 2023, *AJ*, **165**, 32

Öberg, K. I., Murray-Clay, R., & Bergin, E. A. 2011, *ApJL*, **743**, L16

Offner, S. S. R., Moe, M., Kratter, K. M., et al. 2023, in *ASP Conf. Ser.* 534, *Protostars and Planets VII*, ed. S. Inutsuka et al. (San Francisco, CA: ASP), 275

O'Neil, K. K., Martinez, G. D., Hees, A., et al. 2019, *AJ*, **158**, 4

Pecaut, M. J., & Mamajek, E. E. 2013, *ApJS*, **208**, 9

Perryman, M. A. C., Brown, A. G. A., Lebreton, Y., et al. 1998, *A&A*, **331**, 81

Phillips, M. W., Liu, M. C., & Zhang, Z. 2024, *ApJ*, **961**, 210

Reiners, A., & Basri, G. 2008, *ApJ*, **684**, 1390

Ruffio, J.-B., Horstman, K., Mawet, D., et al. 2023, *AJ*, **165**, 113

Ruffio, J.-B., Konopacky, Q. M., Barman, T., et al. 2021, *AJ*, **162**, 290

Ruffio, J.-B., Macintosh, B., Konopacky, Q. M., et al. 2019, *AJ*, **158**, 200
 Schlecker, M., Burn, R., Sabotta, S., et al. 2022, *A&A*, **664**, A180
 Schwarz, H., Ginski, C., de Kok, R. J., et al. 2016, *A&A*, **593**, A74
 Service, M., Lu, J. R., Campbell, R., et al. 2016, *PASP*, **128**, 095004
 Shkolnik, E., Liu, M. C., & Reid, I. N. 2009, *ApJ*, **699**, 649
 Snellen, I., Brandl, B., de Kok, R., et al. 2014, arXiv:1404.7506
 Tannock, M. E., Metchev, S., Heinze, A., et al. 2021, *AJ*, **161**, 224
 Theissen, C. A., Burgasser, A. J., Martin, E. C., et al. 2022, *RNAAS*, **6**, 151
 Tokovinin, A., & Moe, M. 2020, *MNRAS*, **491**, 5158
 Tremaine, S. 1991, *Icar*, **89**, 85
 Veras, D., Crepp, J. R., & Ford, E. B. 2009, *ApJ*, **696**, 1600
 Wang, J., Kolecki, J. R., Ruffio, J.-B., et al. 2022, *AJ*, **163**, 189
 Wang, J. J., Ruffio, J.-B., Morris, E., et al. 2021, *AJ*, **162**, 148
 West, A. A., Hawley, S. L., Bochanski, J. J., et al. 2008, *AJ*, **135**, 785
 Wilcomb, K. K., Konopacky, Q. M., Barman, T. S., et al. 2020, *AJ*, **160**, 207
 Wizinowich, P. 2013, *PASP*, **125**, 798
 Wright, J. T., & Howard, A. W. 2009, *ApJS*, **182**, 205
 Xuan, J. W., Wang, J., Finnerty, L., et al. 2024, *ApJ*, **962**, 10
 Xuan, J. W., Wang, J., Ruffio, J.-B., et al. 2022, *ApJ*, **937**, 54
 Yelda, S., Lu, J. R., Ghez, A. M., et al. 2010, *ApJ*, **725**, 331
 Zapatero Osorio, M. R., Martín, E. L., Bouy, H., et al. 2006, *ApJ*, **647**, 1405
 Zendel, M., Lebzelter, T., & Nicholls, C. P. 2023, *A&A*, **679**, A57